We like to thank the reviewers very much for reading our manuscript so carefully and for providing very detailed comments which helped us indeed to further improve the manuscript Please find our detailed point-to-point replies to all comments below in *italic and blue*. All changes are marked in the following document. The page and line numbers given below refer to this red-lined version.

Point-by-point response to reviewer #1

General comments:

The study introduces a lidar forward operator in order to simulate the expected lidar observations corresponding to output from a dispersion model such as COSMO-ART, allowing for more direct comparison between the model output and lidar observations from instruments such as CALIOP or automated ceilometer lidar systems. Rather than using a fixed lidar ratio, the new forward operator calculates the scattering properties of the particle mixture specified by the dispersion model. The COSMO-ART simulation of the 2010 Eyjafjallajökull eruption is used as a case study.

The computationally efficient method for calculating the aerosol scattering properties, backed up by sensitivity studies, and the flexibility of the resulting model make this work an important contribution.

Thank you very much for this positive comment on our work!

The writing style is very clear, but could be more succinct: some of the background information seems unnecessarily detailed and detracts from the focus of the study.

Agreed. We rechecked the whole manuscript for aspects which could be shortened, removed or rewritten in a clearer way, see comments below. The revised manuscript is now much more succinct with a better focus on the focus of the presented backscatter lidar forward operator study.

Specific comments:

Page 2, lines 1-24. This discussion of different dispersion models and different lidar configurations doesn't come up much later in the manuscript. Is it possible to tie the most relevant aspects more closely to the focus of the study, and omit the rest?

Thank you, we agree. We removed the detailed information about existing forward operators but kept literature references to provide a link to this background information (p.3, lines 13-27)

Page 3, lines 1-12. Does each of these lidar forward operators simulate CALIOP, a ground-based lidar network, or both?

Thank you for raising this question, which helps us to clarify this point. As we have removed the description of the forward operators as suggested by the reviewer above, we did not add this clarification in the revised manuscript but answer this question here: The first mentioned forward operator developed at ECMWF was designed for (satellite-mounted) MODIS (Benedetti, 2009), the second for (also satellite-mounted) CALIOP. The forward operator of SIĈ (2014) is more generic and can be configured for both ground-based and satellite-based measurement instruments. The forward operator of Charlton-Perez et al. (2013) is for ground-based automated lidar devices.

In principal, an ideal lidar forward operator can be configured to any lidar measurement geometry, i.e. ground-based, satellite-based, vertically-measuring (also at variable zenith angle). This information was also added to the manuscript (p. 3, lines 11-12 in the document with changes marked).

Pages 4-11. The equations that are not new to this study should have sources cited; the better-known aspects of lidar physics can probably be described more briefly.

Thank you for this comment. We agree and have removed redundant information, see p. 5 l. 15-19., p. 7 l. 2-3, p. 9 l. 11-12, and p. 10 l. 1-4. Section 2 is now much clearer and focused on the basic principles of the forward operator without omitting relevant information.

Page 8, lines 2-7. Likewise, the substitution of sums for integrals in the numerical computation is straightforward enough that I'm not sure we need the steps spelled out explicitly.

We agree and have removed the mentioned equations.

Page 10, line 11. For Fig. 1, can you overlay the track of the CALIPSO overpass you show in Fig. 3? It would be helpful to connect the overhead and profile views of the ash plume.

Very good idea. Thank you. The track of CALIPSO was overlaid in Fig. 1 as suggested.

Page 18, lines 1-6. The "missing" ambient boundary-layer aerosol seems as if it would also make quantitative comparison very difficult.

Thank you, this is indeed the case and mentioned in Section 5.3, p. 20 l. 18-25.

Technical comments:

Page 1, line 20. By "aerosol cloud movements" do you mean the movement of aerosol and clouds, or of aerosol plumes?

Thank you. Clarified. We mean aerosol/volcanic ash plumes and therefore we replaced "aerosol cloud" throughout the manuscript.

Page 5, lines 3-5. This sentence is unclear.

Clarified. The paragraph was rewritten to focus on its intended expression (p. 5, l. 15-19).

Page 7, line 1. Should be "Mie scattering-related"

Agreed. We changed the manuscript accordingly.

Page 10, line 10. "Spatial extent"

Page 17, line 1. "Predominantly"

Page 17, line 4. Should be "This may be important information"

Page 20, line 16. "A comparison of the volcanic ash signal"; "was too high"

Thank you for reading the manuscript so carefully! We fixed all of these points in the revised manuscript

Point-by-point response to reviewer #2

General comments:

The paper presents a new backscatter-lidar forward operator based on the distinct calculation of the aerosol backscatter and extinction properties. This operator was then applied to a specific case study: the Eyjafjallajökull eruption in 2010. It is noted the importance of developing a forward operator based not on a fixed lidar ratio. This approach is really valuable and could have significant impact on future data assimilations schemes. The paper is generally clearly written and the topic is suitable for AMT. However there are still aspects to be better exploited before the paper can be accepted for publication on AMT.

We thank the reviewer for his positive comment on the importance of our work and our scientific approach. As suggested by the reviewer, we have extended the discussion and include now also measurements of multi-wavelength Raman lidar systems as high-quality reference data for verification (see details below).

I understand that the chosen case study is considered suitable because in case of a volcanic eruption the source is known and very limited in space and time. However, it is well known that volcanic ash particles are not spherical and this increase the complexity of the case study. The authors have addressed this issue using, in a second step, the T-matrix approach for sensitivity studies and they consider this approach sufficient. Probably this statement should be better analysed.

We fully agree and thank the reviewer for supporting our approach. We are happy to give more details. As many types of aerosol particles are non-spherical in nature, one has to face this and develop and investigate critically different approaches to cope with the high complexity of scattering processes in nature. We fully agree and like to clarify that we certainly do not consider our approach as finally "sufficient". We only believe that the critical discussion of our new approach and its uncertainties will be helpful for other scientists facing just the same problems in stepwise improving our knowledge in how to deal with the important task of aerosol monitoring and modeling in the future – also including soon refined related data assimilation techniques. We added this further clarifying statement in the conclusions section (p. 22, l. 21-25, p. 23 l. 1-4).

Please note that in the existing literature there is so far no estimation or quantification of the errors at all regarding the existing forward operators which are all based on the assumption of a fixed lidar ratio. We therefore see our approach as very interesting contribution for current and future lidar forward operators similar to the error estimation which is performed for measured data. As suggested by the reviewer, we explain this now further in the revised manuscript (p. 25, l. 30 to p. 26 l. 3).

In particular, I'd suggest to reduce as much as possible the other error sources. Limitation for particles larger than 10 micron cannot be reduced (see also Madonna et al. JGR 2013, 10.1002/jgrd.50789), because it is intrinsic in the lidar technique (even if with larger wavelength, as in the case of ceilometers, the sensitivity improves but it is not sufficient for this particle size range).

We are thankful for the hint on this valuable reference. The results of Madonna et al. (2013) are in good agreement with our findings (see e.g., section 5.2 where the relative mass contribution and relative contribution to the forward modeled attenuated backscatter coefficient at two locations were analyzed for the 6 volcanic ash size classes). The reference was added to section 5.2 as validation reference and a sentence was added which mentions the reduced sensitivity of ACL systems for "giant" and "ultragiant" particles (p. 19, l. 30).

On the other side calibration errors and eventual presence of aerosol background could be reduced using data from a Raman lidar or HSRL.

Certainly, we fully agree with the reviewer (and one of us, Andreas Behrendt, is working with Raman lidar development and data analysis since more than 20 years). But unfortunately even though there are networks like EARLINET and even a few automatic Raman lidar systems, the data density is still low, the data are unfortunately so far mostly limited to nighttime observations only, the measured data is not yet available – especially not in real time – all points which make the data of ceilometer networks still very attractive and it worthwhile to consider/evaluate this much denser data set for aerosol monitoring – certainly having in mind that future automated Raman lidar networks will provide even better data. The forward operator provides the attenuated backscatter coefficient directly from model output data without the need for calibration.

We also fully agree that the ACL calibration using satellite-based measurements of CALIPSO is of course related to the mentioned uncertainties. We therefore extended the study and include now also multi-wavelength Raman lidar measurements from Munich and Leipzig (Ansmann et al., 2010) as additional reference which revealed that the applied calibration was indeed within the uncertainties, see sect. 3.2 in the revised manuscript (p. 13 l. 4-10). Due to the distance between ACL station Deuselbach and Munich/Leipzig, we can of course not expect that the planetary boundary layer aerosols have the same composition and number-density as above the ceilometer in Deuselbach. It is noteworthy in this context that the need of quantitative calibration of the ceilometer systems was meanwhile accepted by the manufacturers and calibrated systems are also available. (p. 13, l. 10-12).

I understand that the Eyjafjallajökull eruption in 2010 was a great opportunity to present the potential of the German ACL network, however in this paper only data from a single ceilometer station are used. I do not see the need to present the network here.

We agree and removed the map showing the ceilometer network in 2010. Instead, the limited availability of useable ACL measurement data of the volcanic plume over Germany was commented in the revised manuscript, section 3.2 (p. 12 l. 7-9).

Actually, even if I understand the interest of using this kind of ceilometers instead of more advanced research lidar (clearly explained in the paper), I do not understand why the comparison with the forward operator is not done first with a more advanced lidar (at least measuring independent extinction and backascatter profile) [Raman lidar o HSRL]. It is not necessary to use a multiwavelength Raman lidar if the authors do not want to, but at least a lidar providing independent extinction and backscatter profiles. This could have helped the assessment of the operator reducing calibration uncertainty and also improving signal to noise ratio at altitude where is more realistic to neglect aerosol background and consider only volcanic particles.

The authors could then perform a sensitivity test in case of ceilometers. I have to say that the smart idea of developing this operator does not fit with the calibration of the ACL with CALIPSO (which is very weak). I suggest a more quantitative approach first and then to try to apply it to simpler lidar as the ceilometers, which I agree, we should better investigate the specific potential because even if more Raman lidar and HSRL are becoming more “operational” the coverage will be never comparable as that we have for the ceilometers.

We fully agree that a comparison with Raman lidar measurement for the given case study would be very interesting for testing the forward operator. However, the only Raman lidar measurements in Germany available were the EARLINET systems at Munich and Leipzig (Ansmann et al. (2010)). As shown in fig. 2 of the original manuscript, the map indicates that none of the systems in east and southeast Germany had full vision to the volcanic ash plume which renders a time-height cross-section comparison between forward operator output and Raman lidar measurement at these stations impractical.

The absolute values reported by the Raman lidar systems at a wavelength of 1064 nm, however, agreed within the measurement uncertainties and expected natural differences in the sampled air mass with the results of the forward operator (see p. 13 l. 4-10), which is quite remarkable given the large uncertainties of the ash data in the model (assumed emission rate of the volcano, atmospheric dynamics, dynamic of the modeled ash plume in the atmosphere including sedimentation etc.) and that there is no data assimilation regarding aerosol data at all yet. As the focus of this study is to critically discuss the potential of ACL networks for data assimilation, further discussions of Raman lidar measurements are beyond the scope of this study but certainly highly interesting in next steps of future studies using the forward operator. In this context also the upcoming ESA satellite sensor EarthCARE with its high-spectral resolution lidar is certainly of high interest.

We added these considerations in the conclusions section (p. 24, l. 28-34).

Specific comments

Probably the reference Matthias et al., atmenvir 2011 should be cited. Extinction profiles simulated with a fixed lidar ratio.

The only lidar-/aerosol-related publication of Matthias et al. in 2011 we found has the title "The ash dispersion over Europe during the Eyjafjallajökull eruption - Comparison of CMAQ simulations to remote sensing and air-borne in-situ observations" and is a valuable reference for the topic of our manuscript even if the authors use parameterized equations proposed by Malmet al. (1994) to calculate the extinction coefficient for a comparison of the aerosol optical depth between CMAQ model and three sources of remote sensing measurement data. We added the reference to section 3.1 (p. 11 l. 27-29).

Fig. 2 reports the distribution of the German ACL network: it is a pity that only 6 stations are reported in green (clean air situation with a full view on the ash layers). This is not commented at all in the text. It should be probably explained or at least mentioned what are the limitation of the use of these instruments (it is only reported that they are more operational respect to research lidar). However as I said previously, I do not see why this network should be presented considering that it is not used in the paper.

We fully agree as mentioned above and removed the whole figure but summarize its essence in section 3.2 (p. 12, l. 7-9).

Calibration of the ACL with CALIPSO is very weak: no ideal co-location, limited signal to noise ratio for the ACL.

We agree and thus enhanced the manual calibration approach by also comparing the results of the forward operator/manually-calibrated ACL data with high-quality 1064 nm Raman lidar measurements taken at Munich and Leipzig and found a good agreement of the absolute values (p. 13 l. 4-10).

Comparison between ACL and the model has no sense in the PBL because only volcanic particles have been considered and here it is not possible to neglect other aerosols (not only in the PBL, looking at the fig 15 and 16 at least up to 2 km of altitude).

We agree and added this important limitation to the description of figure 13 in the revised manuscript (p. 50).

The ACL signal is too noisy between 4 and 8 km of altitude where a much more realistic comparison with the model could have been done considering only volcanic particles.

We agree that the ACL signal is noisy – as already mentioned in the text. There is, however, a wide vertical range left which offers great potential for comparison between ACL measurement and forward operator output, namely heights between 2 and 8 km ASL: In this height range, the instrument has reached full overlap yet, background aerosols are available at very limited concentration and the instrument noise is low enough to accentuate the volcanic ash plume in the forward modeled lidar profiles. We added this information to the description of figure 13 in the revised manuscript (p. 50).

Future comparisons of Raman-lidar-measured particle-only backscatter and extinction profiles with particle-only forward modeled backscatter and extinction profiles would increase the contrast in these heights even more by omitting the molecule signal. The mentioned problem of background aerosol in the planetary boundary layer, however, can only be solved by implementing such aerosols into the dispersion model and representing their contribution by the forward operator.

It is unrealistic to calibrate at 3 km of altitude supposing only molecular contribution at this altitude in Central Europe (Pag 11, line 16).

We agree and removed this component of the manual calibration approach from the text (sect. 3.2) as the newly added Raman lidar reference values are much more trustworthy (p. 13, l. 4-10).

The comparison with a much better calibrated lidar is recommended. There should be many Raman or HSRL data available for the considered case study which could be used for this comparison.

As above, we fully agree and added respective comparisons to the manuscript.

To use better calibrated lidar data would have allowed a better quantitative comparison, as also mentioned by the authors. I strongly recommendthe authors to use this kind of data for the comparison with the model. Then, once the operator is better assessed could be exported to the specific case of ceilometers.

Certainly. It should be mentioned, however, here that the comparison between forward operator output and lidar measurement was not intended to validate the forward operator. Differences between the forward operator results and lidar measurement are due to: missing aerosol types (p. 25 l. 12-14), errors of the model prediction (p. 23 l. 25-32), uncertainties of the particles' scattering properties in the forward operator (p. 22 l. 217 – p. 23 l. 4 […]) and measurement errors (p. 23 l. 33 – p. 24 l. 3). If the model prediction is quite uncertain or does not deliver all required information (such as the missing background aerosol), an improvement of the measurement data quality (as proposed here) does not result in a situation which allows for validating the forward operator. The forward operator – as a mathematical description for a physical process – should preferably be validated by proofing its concept and implementation.

Pag 3 line 15, extinction less sensitive to dimension and shape, but not on refractive index

We have changed the sentence to "is less sensitive to the particle dimension and shape".

Pag. 10, lines 1-3: there are many lidar ratio data available for this case. Please add appropriate references. The authors state here "missing reference measurement data" which is in contrast with what reported at pag. 19, line 31.

We fully agree as we have referenced lidar ratio values from this case. Thus, the mentioned sentence was deleted from the manuscript.

Page 20 lidar ratio di 5sr?? this value is completely out of the range of values observed in case of volcanic ash.

Certainly, we are well aware of this. But please note that these values are the lidar ratio values of each individual volcanic ash size class and not the composite. To better clarify the definition of the lidar ratio, we now differentiate the measured lidar ratio, the total lidar ratio and the "pure" lidar ratio in the manuscript. The Section "Lidar ratio" was therefore completely rewritten (p. 10 l. 12 to p. 11, l. 12).

From this definition, we calculated the total lidar ratio at two sample coordinates; see Table 4 and Table 5. The total calculated lidar ratio values were 9.63 sr, and 46.53 sr, respectively. From an analysis of the pure lidar ratio, we found indications that the particle size class configuration for the small particles < 1 µm could have a huge impact on the calculated total lidar ratio. But we also found that spherical particles have the lowest pure lidar ratio value of all considered shapes for the particle sizes between 0.5 µm and 3.5 µm as well as between 4 µm and 6 µm in radius. This is in good agreement to the results of the backscatter cross section sensitivity studies where the effective backscatter coefficient of spherical particles within size classes 1, 2, and 3 was shown to be higher than of any other concerned particle shape (up to factor 5). Please note that our results are also in good agreement to Gasteiger et al.: Modelling lidar-relevant optical properties of complex mineral dust aerosols. The authors found pure lidar ratio values of 5 sr to 20 sr even for irregularly-shaped particles as mentioned in our manuscript (p. 23, l. 9-13).

From this analysis, we were able to relate differences between measured and calculated lidar ratio to consequences of the assumption of spherical particles and to the models' volcanic ash size class configuration but further investigation is required in this topic to optimize both the particle size class configuration as well as the volcanic ash representation in the forward operator. We added this analysis to the manuscript (p. 23, l. 5-24).

Figures are not generally sufficiently commented.

We agree and extended the figure description and added comments to all figures to give the reader a better understanding of the shown content.

References to relevant papers and important programmes in the field are omitted. Considering ceilometers networks, it is suggested to mention E-Profile at least in the conclusion.

It was not our intension to omit anybody. We fully agree that these ongoing research programmes are interesting in this context and added a paragraph related to E-Profile and EARLINET and their contributions in the conclusions section (p. 25, l. 30-33).

Sections 2-4 could be more succinct.

We scanned the whole manuscript and removed contents with less relevant information. Some paragraphs have been removed while others have been rewritten to make their meaning even more obvious and succinct. All changes are highlighted in a supplement document created using latexdiff.

Technical comments:

- The acronym "ACL" is reported in the abstract where it is not explicitly explained
- Page 17, line 1. "Predominantly"
- Pag. 20, line 16: A comparison "with" the volcanic . . .

Thanks! The wording issues mentioned above were applied to the manuscript.

- Please check the quality/resolution for fig. 2

Done but according to the suggestion above, fig. 2 was removed from the manuscript due to its limited relevance for the manuscript.

-Figures 5 and 6: The readability of the text should be improved

Done. To improve the readability, we applied anti-aliasing of fonts and lines which significantly improved the appearance and readability of the plot and text fields; see the comparison below (Fig. 1 and Fig. 2 in this document). A further increase of the readability (increase of text size) seems not to be reasonable because this would result in a reduction of both tick and label numbers.

- Figures 7-8-9-10: axis labels should be enlarged

Done. We reworked the particle shape sensitivity study figures. First, text size was increased and the axis labels have been rescaled for figures 7-8-9-10-11-12. Also, the summary figures for the relative difference of the effective values of spheres and non-spherical scatterers have been improved by showing ellipsoids and cylinders using separate panels; see fig. 10 and 11 in the revised manuscript.

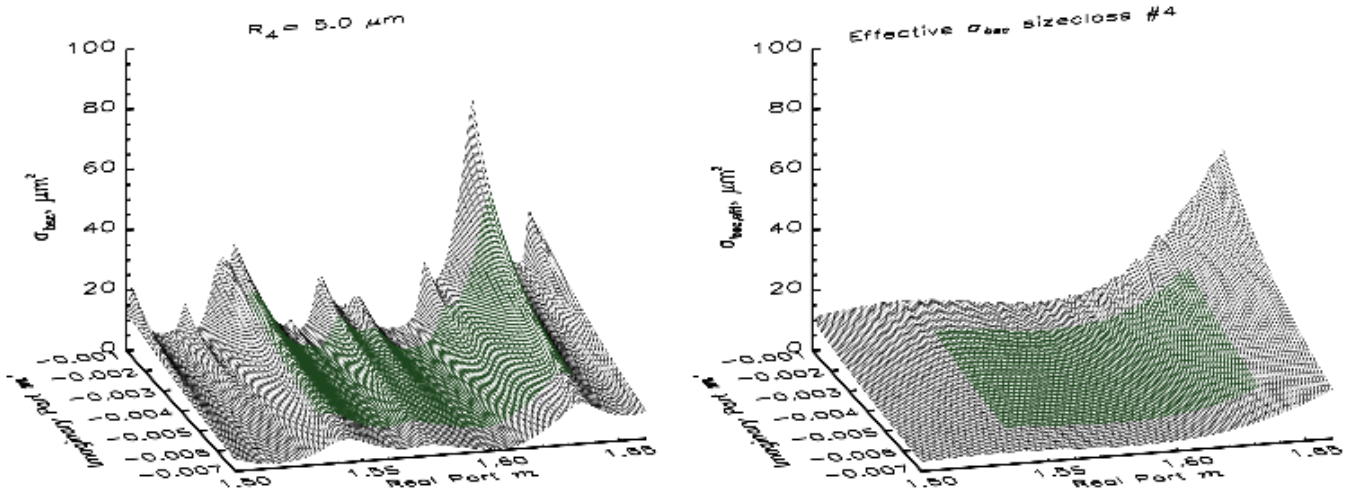

Fig. 1: Non-anti-aliased fig. 6 of the manuscript (before)

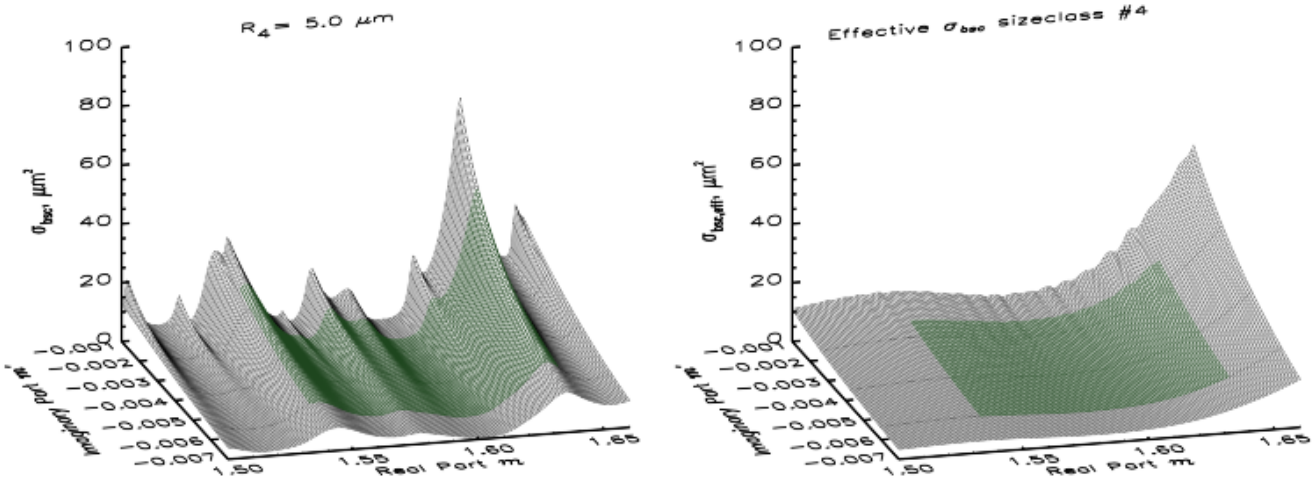

Fig.2: Anti-aliased fig. 6 of the manuscript (after)

Development and Application of a Backscatter Lidar Forward Operator for Quantitative Validation of Aerosol Dispersion Models and Future Data Assimilation

Armin Geisinger[1], Andreas Behrendt[1], Volker Wulfmeyer[1], Jens Strohbach[1], Jochen Förstner[2], and Roland Potthast[2]

[1]Institute of Physics and Meteorology, University of Hohenheim, Germany.
[2]Headquarter of the German Weather Service, Offenbach, Germany

Correspondence to: Armin Geisinger (armin.geisinger@uni.hohenheim.de)

Abstract.

A new backscatter-lidar forward operator was developed which is based on the distinct calculation of the aerosols' backscatter and extinction properties. The forward operator was adapted to the COSMO-ART ash dispersion simulation of the Eyjafjallajökull eruption in 2010. While the particle number concentration was provided as model output variable, the scattering properties of each individual particle type ~~had to be determined by extensive~~ were determined by dedicated scattering calculations. Sensitivity studies were performed to estimate the uncertainties related to the assumed particle properties. ~~Therefore, scattering~~ Scattering calculations for several types of non-spherical particles required the usage of t-matrix routines. Due to the distinct calculation of the backscatter and extinction properties of the models' volcanic ash size classes, the sensitivity studies could be resolved to each size class individually which is not the case for forward models based on a fixed lidar ratio. Finally, the forward modeled lidar profiles have been compared to ~~ACL~~ automated ceilometer lidar (ACL) measurements both qualitatively and quantitatively while the attenuated backscatter coefficient was chosen as ~~common~~ suitable physical quantity. As the ACL measurements were not calibrated automatically, their calibration had to be performed using ~~CALIPSOs/CALIOP~~ satellite lidar and ground-based Raman lidar measurements. A slight overestimation of the model predicted volcanic ash number density was observed. ~~By manually reducing the model predicted ash number density, the effect of simple data assimilation methods could be demonstrated. Major issues~~ Major requirements for future data assimilation of ~~ACL data~~ data from automated ceilometer lidar (ACL) have been identified, namely, the availability of calibrated lidar measurement data, a scattering database for atmospheric aerosols, a better representation and coverage of aerosols by the ash dispersion model and more investigation in backscatter lidar forward operators where the backscatter coefficient is calculated directly and for each individual aerosol type. The introduced forward operator offers the flexibility to be adapted to a multitude of model systems and measurement set-ups.

1 Introduction

In Spring 2010, the ~~volcano~~ Icelandic volcano Eyjafjallajökull erupted several times. The emitted ash was found to be harmful for aircraft and due to uncertain information about spatial distribution and concentration of volcanic ash, the European air space was closed for several days (Sandrini et al., 2014). The high economic costs and impact on public transport lead to efforts of DWD (Deutscher Wetterdienst) to improve at monitoring and predicting ~~aerosol cloud movements~~ ash plumes in the atmosphere. Therefore, DWD decided to start a dedicated project on backscatter lidar forward operators for validating aerosol dispersion models using available ~~remote sensing measurement data~~ remote-sensing measurement data and for future assimilation of lidar backscatter and extinction data.

Atmospheric chemistry models which allow for aerosol dispersion predictions are, amongst others, COSMO-ART (Consortium for Small-scale Modeling, Aerosols and Reactive Trace gases, Vogel et al. (2009)), COSMO-MUSCAT (Multiscale Chemistry Aerosol Transport, Wolke et al. (2004)), ECMWF (European Center for Mesoscale Weather Forecast, Benedetti (2009), ENVIRO-HIRLAM (Environment - High Resolution Limited Area Model, Zakey et al. (2006)), MACC-II (Monitoring Atmospheric Composition and Climate - Interim Implementation, Cuevas et al. (2015)), MCCM (Multiscale Coupled Chemistry Model, Emeis et al. (2011)), MesoNH (Non-Hydrostatic Mesoscale Atmospheric Model of the French ~~research community~~Research Community, Mallet et al. (2009)), WRF-CHEM (Weather Research and Forecast Model, Chen et al. (2014)). Using these model systems, scientists have analyzed the aerosol influence on, for example, precipitation (Rieger et al., 2014), temperature (Bangert et al., 2012), radiative fluxes ~~(Vogel et al., 2009; Chaboureau et al., 2011).~~ (Vogel et al., 2009), and convection initiation (Chaboureau et al., 2011). These models are potentially capable of simulating such ash dispersion scenarios and could thus benefit from the methodology presented here.

Lidar (light detection and ranging) is capable of providing information on atmospheric particles with high temporal and spatial resolution. The most basic lidar type is the backscatter lidar which measures the backscattered signal intensity of a volume at a certain range. Comparing the data of such a backscatter lidar that is operated in the UV with simulations of an atmospheric chemistry model, allows, e.g., for the characterization of transport and optical properties of aerosol particles near sources (Behrendt et al., 2011; Álvaro M. Valdebenito B et al., 2011). Using ground-based DIAL (differential absorption lidar, Dagan (2008); Späth et al. (2016)) water-vapor can be measured, which can even be combined with backscatter measurements to derive more details of aerosol particle properties (Wulfmeyer and Feingold, 2000). Lidar techniques based on the vibrational and rotational Raman effect, like RRL (rotational Raman lidar) allow for the measurement of trace gas profiles ~~(Whiteman et al., 1992; Turner et al., 2002; Wulfmeyer et al., 2010)~~(Whiteman et al., 1992; Turner et al., 2002; Wulfmeyer et al., 2010; H as well as profiles of atmospheric temperature, particle backscatter cross section, particle extinction cross section, and particle depolarization properties (Behrendt et al., 2002; Hammann et al., 2015; Radlach et al., 2008). HSRL (high spectral resolution lidar) systems furthermore allow for cloud and particle characterization (Shipley et al., 1983). ~~Multiwavelength~~ Multi-wavelength lidar systems offer the potential to retrieve the optical, microphysical and chemical properties of aerosols (Mamouri et al., 2012) but these systems are rare and the inversion algorithms are very complex. Profiles of the radial wind speed can be obtained by Doppler-Lidar systems, e.g., Banta et al. (2012).

While the number of sophisticated lidar instruments that provide thermodynamic data (Wulfmeyer et al., 2015) is still low, there are already automated aerosol lidar networks in operation in Europe and Asia (Pappalardo et al., 2014; Sugimoto et al., 2008). ~~For example the German weather service (Deutscher Wetterdienst, DWD) maintained already in 2010 a network of about 36 automated ceilometer lidar (ACL) systems (Flentje et al., 2010a).~~ The data of such a network offers 3D particle information with a high temporal, high vertical, and a moderate horizontal resolution. ~~The ACL systems~~ Automated ceilometer lidar systems (ACL) have been used to detect cloud and boundary layer heights (Emeis et al., 2009) but the received signal delivers also information about aerosols. It is therefore worthwhile to use the ACL network measurements for the validation of particle transport model simulations. Unfortunately, it is not possible to obtain the particle number concentration from an elastic backscatter signal alone without ancillary information and assumptions which are partly critical. The ~~preferable way is thus to use~~ alternative way is using the detailed atmospheric description of the model to simulate lidar profiles for a model-given atmospheric state. ~~Then, the quantitative comparison can be performed between the simulation and observation more accurately.~~ Such a lidar simulator is called lidar forward operator. Using an ideal lidar forward operator, the signal of a given lidar system can be calculated from the model prediction at any time interval, grid location, and measurement direction.

There are already several backscatter lidar forward operators available or in development ~~. At ECMWF (European Centre for Medium-Range Weather Forecasts), a lidar forward operator was developed and tested in an ice cloud scenario (Benedetti, 2009), based on assumptions concerning the lidar ratio S_{lidar}. Newer implementations of the ECMWF model allow for simulating the backscatter coefficientmeasurement of the satellite-mounted CALIOP (Cloud-Aerosol Lidar with Orthogonal Polarization) at two wavelengths 532 nm and 1064 nm for spherical sea salt and mineral dust particles (Morcrette et al., 2009). The lidar forward model of SIČ (2014) has the capability to calculate the atmosphere optical depth (AOD) and the particle extinction coefficient from simulations of the CTM MOCAGE (Chemical-Transport Model, Modèle de Chimie Atmosphérique à Grande Echelle). But similar to the ECMWF forward operator, assumptions on the~~ which are based on the calculation of the extinction coefficient. The backscatter coefficient is then calculated from assuming a given lidar ratio S_{lidar} ~~are mandatory to calculate the particle backscatter coefficient. At MetOffice, UK, a backscatter lidar forward model is being investigated (Charlton-Perez et al., 2013) whic considers clouds, one type of aerosol, and rain simulated by the Unified Model (UM). Another lidar forward model is being developed for the EURAD-IM (European Air Pollution and Dispersion – Inverse Model, Lange and Elbern (2014)), but no published results have been found in literature. Consequently, all existing lidar forward operators which we found in literature calculate only the extinction coefficient. The backscatter coefficient, however, is not calculated explicitly for given atmospheric scatterer species.~~ (Benedetti (2009); Morcrette et al. (2009); SIČ (2014); Charlton-Perez et al. (2013); Lange and Elbern (2014)). On the one hand, this method benefits from the fact that the extinction coefficient is less sensitive to the particle ~~properties~~ dimension and shape than the backscatter coefficient. On the other hand, the precision of this method is limited to the correctness of assumed lidar ratio values. The method becomes furthermore unusable once there is a mixture of scatterers~~for which the effective lidar ratio is not known. To become independent on the assumption of a lidar ratio, we~~ .

We designed a forward operator which is based on the ~~independent calculation of both the~~ distinct calculation of extinction and the backscatter coefficients ~~.~~

~~Our~~ in the model system. This forward operator can be adapted to ~~any~~ particle-representing atmospheric model ~~system~~ and backscatter lidar ~~system~~ systems even using multiple wavelengths. ~~The forward operator is optimized~~ It has the capability to calculate both the attenuated backscatter coefficient and the lidar ratio from model output data with a minimum set of external information. ~~We call this forward model the~~ The name of the forward model is "backscatter lidar forward operator" (BaLiFOp). ~~This forward operator is planned to be used for particle data assimilation.~~

~~Within its priority project KENDA (Kilometer-Scale Ensemble Data Assimilation) the COSMO Consortium has developed an Ensemble Kalman Filter for data assimilation on the convective scale. It is scheduled for introduction into operational use by MeteoSwiss and DWD in 2016. An advantage of the ensemble data assimilation system is that the assimilation can be carried out based on the pure forward operator, and that it is not necessary to calculate derivatives of the forward operator or the adjoint tangential model for carrying out data assimilation. Also, it naturally introduces model increments for all variables where some dynamic covariance is observed from the underlying ensemble model runs. DWD aims to test the assimilation of ACL data into the COSMO-ART model based on the BaLiFOp Lidar forward operator. Here, the current work is a necessary and important basis for further work to improve numerical weather prediction and particle forecasting.~~

In the following we explain the lidar principles and the theoretical background for the backscatter lidar forward operator (Sect. 2). This is followed by an introduction to the case study in Sect. 3. Sensitivity studies of the particles' scattering properties are presented in Sect. 4. Results of the forward operator and a comparison to ACL measurement data are shown in Sect. 5. Finally, we summarize the results of our study and discuss both the benefits and the requirements of ~~ACL~~ current and future lidar data assimilation systems (Sect. 6).

2 Methods

2.1 The Lidar Equation

The lidar principle is based on the emission of ~~UV, visible or IR~~ laser pulses into the atmosphere and the measurement and analysis of the backscatter signals. The received photon number per pulse $N_{\mathrm{rec},\lambda}(z)$ from range z is described by the following equation for elastic backscatter lidars which detect the backscatter signal at the emitted wavelength

$$N_{\mathrm{rec},\lambda}(z) = N_{\mathrm{tr},\lambda} \frac{\tau c}{2} \eta_\lambda \, O(z) \, \frac{A_{\mathrm{tel}}}{z^2} \, \beta_\lambda(z) \, \exp\left(-2 \int_0^z \alpha_\lambda(z') \, dz' \right). \tag{1}$$

Instrument-dependent variables of the lidar equation are the wavelength λ, the laser emitted photon number per pulse $N_{\mathrm{tr},\lambda}$, the temporal length of a laser pulse τ, the ~~speed of light c, the~~ efficiency of the receiving system and detectors η_λ, the overlap function $O(z)$, and the net area of the receiving telescope A_{tel}. The received signal intensity can be given either as power or in photon counts. Here, we use photon counts per laser pulse unless otherwise noted.

The range resolution is ~~related~~ usually matched to the temporal resolution of the data acquisition system by $\frac{\tau c}{2} = \Delta z$ with c as speed of light. Typical Δz values for ACL systems are a few meters. The overlap function $O(z)$ is zero (no overlap) near ground and becomes 1 (full overlap) above a certain height which is typically $200\,\mathrm{m}$ to $1500\,\mathrm{m}$ above ground for ACL systems

(Wiegner et al., 2014; Flentje et al., 2010a). The missing overlap limits the capability to measure and calibrate in near range but has no effect ~~on heights~~ where full overlap has accomplished. Heights where $0 < O(z) < 1$ can be overlap-corrected if the device specific overlap function is known.

Processes in the atmosphere are described by the backscatter coefficient $\beta_\lambda(z)$ and the extinction coefficient $\alpha_\lambda(z)$. The backscatter coefficient $\beta_\lambda(z)$ ~~describes~~ is the scattering strength into the direction of the receiving telescope and depends on ~~the wavelength, the~~ wavelength, type, shape and size of scatterers, and their respective number-concentrations; $\beta_\lambda(z)$ is given in units of $\mathrm{m}^{-1}\,\mathrm{sr}^{-1}$. The extinction coefficient $\alpha_\lambda(z)$ is a description for ~~the light absorption and light~~ laser radiation absorption and scattering capabilities of objects in a volume; it is given in units of m^{-1}.

Elastic backscatter lidar systems do not allow for ~~the~~ a separate measurement of $\beta_\lambda(z)$ and $\alpha_\lambda(z)$ as two unknowns cannot be determined with one measured variable. For calibrated backscatter lidar systems, it is thus convenient to calculate the attenuated backscatter coefficient $\gamma_\lambda(z)$ from the measured profiles

$$\gamma_\lambda(z) = \beta_\lambda(z)\, \exp\left(-2 \int_0^z \alpha_\lambda(z')\, dz'\right). \tag{2}$$

It is given in units of $\mathrm{m}^{-1}\,\mathrm{sr}^{-1}$. The attenuated backscatter coefficient is independent of all instrument-specific parameters except the wavelength. Therefore, it is the best suitable physical quantity for a comparison between ~~ACL~~ backscatter lidar measurement and aerosol model using a forward operator as long as no ACL measurements of extinction and backscatter cross section profiles are available for this purpose.

2.2 The Backscatter Lidar Forward Operator

According to Eq. (2), the basic ~~task~~ functionality of the forward operator is ~~to calculate the~~ the calculation of extinction coefficient $\alpha_\lambda(z)$ and backscatter coefficient $\beta_\lambda(z)$ based on ~~the atmospheric state simulated by a model. Knowing the extinction coefficient of a vertical column allows for the solution of the two-way-transmission integral~~ a given atmospheric state and, finally, to determine the attenuated backscatter coefficient $\gamma_\lambda(z)$. ~~In the following, we describe our method of calculating the attenuated backscatter coefficient from a given set of atmospheric scatterer data.~~

2.2.1 Scattering of ~~Light~~ Laser Radiation by Arbitrary Objects

~~If there are q_s different types of scatterers in an illuminated volume, the~~ The total extinction coefficient $\alpha_\lambda(z)$ and the total backscatter coefficient $\beta_\lambda(z)$ ~~are calculated with~~ of an illuminated volume with q_s different types of scatterers are calculated by

$$\alpha_\lambda(z) = \sum_{i=1}^{q_s} \alpha_{i,\lambda}(z) = \sum_{i=1}^{q_s} \int_0^\infty n_i(R,z)\, \sigma_{\mathrm{ext},i,\lambda}(R)\, dR, \tag{3}$$

$$\beta_\lambda(z) = \sum_{i=1}^{q_s} \beta_{i,\lambda}(z) = \sum_{i=1}^{q_s} \int_0^\infty n_i(R,z) \left(\frac{d\sigma_{\mathrm{sca},i,\lambda}(R)}{d\Omega} \right)_\pi dR, \tag{4}$$

where $n_i(R,z)$ is the number-size distribution of scatterer type i at range z given in units of m^{-3}, $\sigma_{\mathrm{ext},i,\lambda}$ is the extinction cross-section of scatterer type i given in units of m^2 with radius R, and $\left(\frac{d\sigma_{\mathrm{sca},i,\lambda}}{d\Omega} \right)_\pi$ is the differential backscatter cross section given in units of $\mathrm{m}^2\,\mathrm{sr}^{-1}$.

For isotropic scattering, the differential backscatter cross section is derived from the scattering cross-section $\sigma_{\mathrm{sca},i,\lambda}(R)$ via

$$\left(\frac{d\sigma_{\mathrm{sca},i,\lambda}(R)}{d\Omega} \right)_\pi = \frac{\sigma_{\mathrm{sca},i,\lambda}(R)}{4\pi\ \mathrm{sr}}. \tag{5}$$

For non-isotropic scattering, a phase function $\phi_{i,\lambda}(\theta,R)$ is used to describe the relative scattering intensity into ~~an~~ angle θ ~~.~~ ~~In the case of monostatic ACL systems, we thus get $\theta = \pi$, giving~~ which is π for monostatic systems:

$$\left(\frac{d\sigma_{\mathrm{sca},i,\lambda}(R)}{d\Omega} \right)_\pi = \frac{\sigma_{\mathrm{sca},i,\lambda}(R)}{4\pi\ \mathrm{sr}}\ \phi_{i,\lambda}(\pi,R). \tag{6}$$

~~In the following, we treat molecule~~ Molecule scattering and particle scattering ~~separately~~are differentiated here, as the respective calculations depend on ~~different~~ suitable physical theories and algorithms.

2.2.2 Scattering by Molecules

~~Assuming that a model distinguishes~~ For a model which is capable to distinguish atmospheric gases such as nitrogen, oxygen, argon, and water vapor, the molecule scattering calculation ~~can~~ could be performed for each individual gas type and molecule size using the Rayleigh theory (Young, 1981). ~~This becomes relevant if inelastic scattering or molecular absorption is involved.~~ For ACL systems, provided that a wavelength is used, which is well outside of molecular absorption lines, the individual gas contribution to the signal does not need to be distinguished.

Consequently, the molecule extinction coefficient $\alpha_{\mathrm{mol},\lambda}(z)$ and the molecule backscatter coefficient $\beta_{\mathrm{mol},\lambda}(z)$ can be calculated with

$$\alpha_{\mathrm{mol},\lambda}(z) = N_{\mathrm{mol},\lambda}(z)\ \sigma_{\mathrm{sca,mol},\lambda}, \tag{7}$$

$$\beta_{\mathrm{mol},\lambda}(z) = N_{\mathrm{mol},\lambda}(z) \left(\frac{d\sigma_{\mathrm{sca,mol},\lambda}}{d\Omega} \right)_\pi, \tag{8}$$

~~The~~ where the molecule number density $N_{\mathrm{mol}}(z)$ is related to the ideal gas law

$$N_{\mathrm{mol}}(z) = \frac{p(z)}{k\,T(z)}, \tag{9}$$

~~where~~

with p ~~is the model prediction of the~~ as atmospheric pressure given in Pascal (Pa), T ~~is~~ as temperature given in Kelvin (K), and k ~~is the~~ as Boltzmann constant which has a value of ~~about~~ $1.381 \times 10^{-23}\,\mathrm{J\,K^{-1}}$.

To calculate the scattering cross-section $\sigma_{\mathrm{sca,mol},\lambda}$ and the scattering phase function $\phi_{a,\lambda}(\theta)$ of air, ~~empirical equations are available. We~~ we used the formulas and look-up tables given by (Buchholtz, 1995). As ~~the~~ these empirical equations are only ~~given~~ provided for wavelengths up to 1000 nm, we simply extrapolated the values to the ACL wavelength in the case study (1064 nm). ~~This method allows us to calculate the scattering properties of air molecules $\sigma_{\mathrm{sca,mol},\lambda}$ and $\left(\frac{d\sigma_{\mathrm{sca,mol},i,\lambda}}{d\Omega}\right)_{\pi}$ directly from model output for a given ACL laser wavelength λ.~~

2.2.3 Scattering by Particles

The scattering characteristics of ~~spheres with sizes not much smaller or larger than the wavelength~~ larger particles are described by Mie's solution of the Maxwell equations (Mie, 1908; Wiscombe, 1980). ~~Methods like the~~ The T-matrix method (Mishchenko et al., 2002) or the discrete dipole approximation (DDA, Draine and Flatau (1994)) allow for ~~scattering calculations~~ calculating the scattering properties of non-spherical objects ~~; again,~~ with sizes not much smaller or larger than the wavelength. ~~The~~ T-matrix ~~algorithm~~ is a tool for computing scattering by single and compounded particles (Mishchenko et al., 2002). It is faster than DDA but limited to rotationally symmetric objects such as ellipsoids, cylinders, or Chebyshev polynomials. DDA, however, ~~can~~ has the flexibility to represent arbitrarily shaped objects at the cost of high computational efforts.

As a rough estimate~~from our studies~~, the computational ~~costs increase~~ time increases by about one order of magnitude when using ~~the~~ T-matrix instead of ~~the Mie approach~~ Mie scattering calculation routines and by another two orders of magnitude when using ~~the~~ DDA instead of ~~the~~ T-matrix~~approach~~. Another increase in computational time is resulting from larger scatterers, i. e., an increase of the particle size ~~causes~~ results in an exponential increase of computing time. ~~We therefore utilize~~ In this study, Mie scattering algorithms are therefore used to perform fast calculations~~although solid particles are in fact non-spherical~~. The effect of scattering by non-spherical particles is analyzed in a second step ~~using the~~ by T-matrix ~~approach for~~ scattering calculations for several non-spherical particle shapes in the frame of sensitivity studies. ~~We consider these approaches as sufficient for the sensitivity studies performed in this work~~This approach is required because the COSMO-ART volcanic plume simulation does not output any information about the particle shape distribution.

~~Mie-scattering related~~ Mie scattering-related computations were performed using the IDL procedure "mie_single", provided by the Department of Atmospheric, Oceanic and Planetary Physics (AOPP), University of Oxford. Input parameters of the procedure are the real part m and imaginary part m' of the refractive index as well as the so-called size parameter $X_\lambda(R)$:

$$X_\lambda(R) = \frac{2\pi R}{\lambda}, \tag{10}$$

where R is the radius of a single particle. The relevant output parameters are the extinction efficiency $Q_{\mathrm{ext},p,\lambda}(R)$ ~~, the scattering efficiency $Q_{\mathrm{sca},p,\lambda}(R)$,~~ and the backscatter efficiency $Q_{\mathrm{bsc},p,\lambda}(R)$ of particle type p. These optical efficiencies are defined as ratio between the optical cross section and the physical cross section:

$$Q_{\mathrm{ext},p,\lambda}(R) = \frac{\sigma_{\mathrm{ext},p,\lambda}(R)}{\pi R^2}, \tag{11}$$

$$Q_{\mathrm{sca},p,\lambda}(R) = \frac{\sigma_{\mathrm{sca},p,\lambda}(R)}{\pi R^2},$$

$$Q_{\mathrm{bsc},p,\lambda}(R) = \frac{\left(\frac{d\sigma_{\mathrm{sca},p,\lambda}(R)}{d\Omega}\right)_{\pi}}{\pi R^2}. \tag{12}$$

As a warning, we would like to point out that the procedure changed its definition of the backscatter efficiency: The ~~current (~~2012 ~~)~~ release of mie_single returns the so-called radar backscatter efficiency which is 4π times the backscatter efficiency as we require it within the forward operator. Furthermore, the procedure expects the imaginary part of the refractive index given as negative number. If positive imaginary part values are used, the procedure runs without showing an error but returns wrong results.

2.2.4 Discrete Particle Number Size Distributions

A major problem of discrete size distributions is the high sensitivity of the optical cross sections to the particle size: A slightly different particle radius may lead to quite a large change of the scattering properties. We present in the following ~~a suggestion~~ an approach to overcome this ~~fundamental~~ problem. Due to the fact that naturally occurring particle size distributions are not discrete, averaging the optical cross sections over certain size-intervals seems straightforward. We will show that this approach indeed reduces the problematic and unrealistic sensitivity significantly. If the model represents only one type of particle, i. e. with a constant refractive index but with discrete radii R_d, we can define the effective extinction cross section and the effective backscatter cross sections with

$$\overline{\sigma_{\mathrm{ext},R_d,m,m',\lambda}} = \frac{1}{R_{d_b} - R_{d_a}} \int_{R_{d_a}}^{R_{d_b}} Q_{\mathrm{ext}}(X_\lambda(R_d), m, m')\, \pi R_d^2\, dR_d, \tag{13}$$

$$\overline{\sigma_{\mathrm{bsc},R_d,m,m',\lambda}} = \frac{1}{R_{d_b} - R_{d_a}} \int_{R_{d_a}}^{R_{d_b}} Q_{\mathrm{bsc}}(X_\lambda(R_d), m, m')\, \pi R_d^2\, dR_d, \tag{14}$$

where R_{d_a} and R_{d_b} are size margins for each particle size class d. These integrals are then exchanged by sums in the numerical computation routines ~~giving~~

$$\overline{\sigma_{\mathrm{ext},R_d,m,m',\lambda}} = \frac{1}{n_{\mathrm{samples}}} \sum_{g=1}^{n_{\mathrm{samples}}} Q_{\mathrm{ext}}(X_\lambda(R_{d_g}), m, m')\, \pi R_{d_g}^2,$$

$$\overline{\sigma_{\mathrm{bsc},R_d,m,m',\lambda}} = \frac{1}{n_{\mathrm{samples}}} \sum_{g=1}^{n_{\mathrm{samples}}} Q_{\mathrm{bsc}}(X_\lambda(R_{d_g}), m, m')\, \pi R_{d_g}^2,$$

~~where n_{samples} is the sampling number and the sampling range $R_{d_b} - R_{d_a}$ is broken down in g subsamples:~~

$$R_{d_g} = g \frac{R_{d_b} - R_{d_a}}{n_{\text{samples}}} + R_{d_a}.$$

~~This~~ The calculation of the effective values is performed for every discrete size class d and - if represented by the model - also for every particle type k.

Consequently, the total particle extinction coefficient $\alpha_{\text{par},\lambda}(z)$ and the total particle backscatter coefficient $\beta_{\text{par},\lambda}(z)$ are calculated from:

$$\alpha_{\text{par},\lambda}(z) = \sum_k \sum_d N_{d,k}(z)\, \overline{\sigma_{\text{ext},R_d,m_k,m'_k,\lambda}}, \tag{15}$$

$$\beta_{\text{par},\lambda}(z) = \sum_k \sum_d N_{d,k}(z)\, \overline{\sigma_{\text{bsc},R_d,m_k,m'_k,\lambda}}. \tag{16}$$

Here, $N_{d,k}$ is the particle number per volume given by the model, $\overline{\sigma_{\text{ext},R_d,m_k,m'_k,\lambda}}$ and $\overline{\sigma_{\text{bsc},R_d,m_k,m'_k,\lambda}}$ are the effective optical cross sections of particle size class d and particle type class k with the respective real part m_k and imaginary part m'_k of the refractive index.

~~This simple solution allows for calculating $\alpha_{\text{par},\lambda}(z)$ and $\beta_{\text{par},\lambda}(z)$ by just solving a few multiplications and summations resulting in a minimal demand of computing time.~~

The forward modeled total extinction coefficient and total backscatter coefficient are the sum of the molecule and the particle extinction and backscatter coefficients:

$$\alpha_\lambda(z) = \alpha_{\text{mol},\lambda}(z) + \alpha_{\text{par},\lambda}(z), \tag{17}$$

$$\beta_\lambda(z) = \beta_{\text{mol},\lambda}(z) + \beta_{\text{par},\lambda}(z), \tag{18}$$

equivalent to Eq. (3) and (4).

2.2.5 Two-Way Transmission

The two-way transmission T_λ is calculated by

$$T_\lambda(z) = \exp\left(-2 \int_0^z \alpha_\lambda(z')\, dz'\right),$$

while T_λ depends on α_λ between the instrument ($z = 0$) and z.

$$T_\lambda(z) = \exp\left(-2 \int_0^z \alpha_\lambda(z')\, dz'\right). \tag{19}$$

Within the forward operator, the two-way transmission is discretized by :

$$T_\lambda(z) = \exp\left(-2 \sum_{z=1}^{n_z(z)} \alpha_\lambda(z)\, \Delta h(z)\, \cos\Theta\right),$$

where the number of height levels between ground and the actual height is expressed by $n_z(z)$, the profile of the extinction coefficient is $\alpha_\lambda(z)$ and the profile of layer thicknesses is $\Delta h(z)$ $\cos\Theta$ with Θ as zenith angle. In the case of forward modeling, a vertically pointing measurement ($\Theta = 0$), the vertical column of model grid boxes at a specific location is required. By changing the zenith angle Θ, the forward operator can also simulate scanning measurements. using the models' vertical layers as height increment and vertical resolution.

2.2.6 Lidar Ratio

Even though the lidar ratio is not measured directly by current ACL systems, the skill capability of simulating the lidar ratio for given scatterer types and scatterer mixtures offers a great potential for sensitivity studies but also for applications comparison to research lidar systems which are capable of measuring this parameter such as Raman lidar.

The The forward modeled total lidar ratio $S_{\text{lidar}}(z)$ in general is defined by the ratio

$$S_{\text{lidar,meas}}(z) = \frac{\alpha_{\text{meas,par},\lambda}(z)}{\beta_{\text{meas,par},\lambda}(z)}.$$

can be calculated from

where $\alpha_{\text{meas,par},\lambda}(z)$ and $\beta_{\text{meas,par},\lambda}(z)$ are the measured

$$S_{\text{lidar},\lambda}(z) = \frac{\alpha_{\text{par},\lambda}(z)}{\beta_{\text{par},\lambda}(z)}, \tag{20}$$

where $\alpha_{\text{par},\lambda}(z)$ and $\beta_{\text{par},\lambda}(z)$ are the total particle extinction and backscatter coefficients which represent the number-size distribution of real scatterers. Assuming a monodisperse number-size distribution ($N_{d,k}$ is a factor), the effective lidar ratio of each size class can be calculated by:

$$\overline{S_{\text{lidar},d,k}} = \frac{1}{R_{d_b} - R_{d_a}} \int_{R_{d_a}}^{R_{d_b}} \frac{\sigma_{\text{ext},d,k\lambda}(R_d)}{\sigma_{\text{bsc},d,k,\lambda}(R_d)}\, dR_d.$$

where $\sigma_{\mathrm{ext},d,k\lambda}$ and $\sigma_{\mathrm{ext},d,k\lambda}$ are the extinction and backscatter cross section of a given by Eq. (15) and Eq. (16), respectively. It depends not only on the assumed particle type and shape, but also on the particle size class d and particle type k. This definition is limited to the scope of monodisperse size classesconfiguration of the model, i.e. the number-size distribution inside a size class is assumed to have a constant value. To calculate the total lidar ratio at distance z, the following equation could be used size class number, size class range and particle size coverage. The forward modeled lidar ratio thus becomes more representative with a wider particle size spectrum as well as more particle size, type and shape classes output by the dispersion model.

To analyze the lidar ratio sensitivity independent of a models' particle size class and type class configuration, we introduced the pure lidar ratio $S_{\mathrm{lidar,pure}}$. In a molecule-free volume with monodisperse particles, the particle number per volume $N_{R,p}$ is a factor with R as particle radius, giving

$$S_{\mathrm{lidar}}(z) = \frac{1}{n_k \cdot n_d} \sum_{k}^{n_k} \sum_{d}^{n_d} N_{d,k}(z)\, \overline{S_{\mathrm{lidar},d,k}},$$

$$S_{\mathrm{lidar,pure},R,p,\lambda} = \frac{\sigma_{\mathrm{ext},R,p,\lambda}}{\sigma_{\mathrm{bsc},R,p,\lambda}}. \tag{21}$$

which has the model predicted number density values $N_{d,k}(z)$ as weight. Due to missing reference measurement data, a comparison of the forward modeled and measured The pure lidar ratio $S_{\mathrm{lidar,pure},R,p,\lambda}$ allows for performing sensitivity studies to analyze influences of the particle shape on the expected lidar ratio values are omitted. The effective lidar ratio values of particles which occur within the case study will be shown in section 5(Sect. 4).

3 Case Study

3.1 Description

The 2010 Eyjafjallajökull eruption was extensively analyzed by scientists from many fields of research, resulting in a substantial knowledge base (see ACP special issue "Atmospheric implications of the volcanic eruptions of Eyjafjallajökull, Iceland 2010"*Atmospheric implications of the volcanic eruptions of Eyjafjallajökull, Iceland 2010*). Ash layers were observed from a large set of measurement instruments, allowing for tracking the volcanic ash cloud movement plume over Europe (Gasteiger et al., 2011a; Zakšek et al., 2013; Mona et al., 2012; Dacre et al., 2013; Waquet et al., 2014). Using images from the geostationary instrument SEVIRI (Spinning Enhanced Visible and Infrared Imager) the spatial extend extent of the ash cloud and its movement plumes and their movements could be tracked and compared to the measurement of ground-based instruments (Strohbach (2015), see Fig. 1). From the synergy of the two measurement systems, signals of the layers with strong backscattering measured by ACL systems could be related to clouds or volcanic ash layers, respectively.

A In terms of dispersion modeling, such a volcanic eruption case is also beneficial for our analysis due to the fact that the ash emission takes place at one geographic location within has a well-known time intervals. Other cases are also interesting

but may lack a precise definition of the test scenario or respective model prediction capabilities, such as the representation of background aerosol or uncertainties of the background aerosol number densityaerosol source location. This feature renders the Eyjafjallajökull eruption an important case study for aerosol dispersion simulation models and respective validation methods (Matthias et al., 2012).

3.2 The DWD ACL Network

ACL networks are the current data source of choice for an analysis of the vertical structure of aerosols. In 2010, the DWD ACL network consisted of 36 systems CHM15k ACL manufactured by Jenoptik now Lufft (see Fig. **??**). a valuable data source for analyzing the vertical and horizontal structure of aerosol particles, model verification, and data assimilation. A qualitative analysis of the ash cloud over Germany with this data set was made Eyjafjallajökull ash plume over Germany using observations from 36 ACL systems CHM15k manufactured by Jenoptik now Lufft was performed by Flentje et al. (2010a).

We used the NetCDF files with ACL raw data where one file contains the 24 hour measurement of one ACL station. From our analysis of the ACL measurements from 14 April 2010 to 16 April 2010, we identified 6 stations where the volcanic ash plume was visible without being tainted by other clouds or hidden by fog layers near-ground.

The received photon number per shot is calculated from

$$N_{\mathrm{rec}}(z,t) = \mathrm{beta\_raw}(z,t) \cdot \mathrm{stddev}(t) + \mathrm{base}(t), \tag{22}$$

where beta_raw is the signal-to-noise measurement product, stddev is noise, and base is a daylight correction provided by the ACL software of this model. The calculation of

The equation for calculating the attenuated backscatter coefficient from ACL data follows Eq. which reads

$$\gamma^*_\lambda(z) = \frac{N_{\mathrm{rec},\lambda}(z,t)\; z^2}{N_{\mathrm{tr},\lambda}\; \eta_\lambda\; A_{\mathrm{tel}}\; O(z)\; \Delta z}.$$

The emitted photon number per shot $N_{\mathrm{tr},\lambda}$ was calculated using:

measured photon counts reads:

$$\gamma_\lambda(z) = \frac{N_{\mathrm{rec},\lambda}(z,t)\; z^2}{N_{\mathrm{tr},\lambda}\; \eta_\lambda\; A_{\mathrm{tel}}\; O(z)\; \Delta z}. \tag{23}$$

where $E_{\mathrm{pulse},\lambda}$ is the laser pulse energy. $E_{p,\lambda}$ is the photon energy, calculated according to:

$$E_{p,\lambda} = \frac{h\; c}{\lambda},$$

with h as Planck's constant having a value of $6.626\,07 \times 10^{-34}\,\mathrm{J\,s}$. The pulse energy of the diode-pumped laser is $8\,\mu\mathrm{J}$ (Flentje et al., 2010b) resulting in an emitted photon number per pulse of about 4.28×10^{13}. The diameter of the receiving telescope is $100\,\mathrm{mm}$ (Flentje et al., 2010b) which results in $A_{\mathrm{tel}} = 78.54\,\mathrm{cm}^2$. The vertical resolution Δz is $15\,\mathrm{m}$ over for the

complete profile. The overlap function $O(z)$ was set to 1 which implies that ranges below about 1500 m cannot be used reliably for comparisons with the forward operator.

Unfortunately, the instruments provided no calibrated measurement data at that time. As the true system efficiency η_λ and the calibration coefficients are not known, we use the symbol η^* as , so a linear calibration factor η^* is used as replacement for the system efficiency η_λ. From a comparison with the calibrated attenuated backscatter measurements of CALIOP at $\lambda = 1064\,\mathrm{nm}$ (Fig. 2), we determined a calibration factor of $\eta^* = 0.003$: First, we used could be determined: Therefore, the CALIOP value of the 1064 nm calibrated attenuated backscatter coefficient was used at 50.15° lat / 4.81° lon in a height of 2 km ASL (about $5 \times 10^{-6}\,\mathrm{m^{-1}\,sr^{-1}}$) to estimate the maximum . As a validation step, the resulting attenuated backscatter coefficient inside values were compared to Raman lidar measurements of the volcanic ash cloud. The second calibration criterion was the forward modeled plume at Munich and Leipzig (Ansmann et al., 2010). The maximum Raman lidar measured backscatter coefficient at $\lambda = 1064\,\mathrm{nm}$ was $8 \times 10^{-6}\,\mathrm{m^{-1}\,sr^{-1}}$ for both Munich and Leipzig and the maximum calculated attenuated backscatter coefficient outside the volcanic ash layer in 3 km ASL which is dominated by molecule scattering and has a value of $1 \times 10^{-7}\,\mathrm{m^{-1}\,sr^{-1}}$, see Fig. 13. This pragmatic approach is of limited precision and only required for uncalibrated ACL measurements. As most of the ACL measurement at Deuselbach after calibration is in the same order of magnitude. As most present ACL networks have been extended by automatic calibration methods after the Eyjafjallajökoll eruption, such a calibration capabilities, such pragmatic calibration approaches will not be required in future forward operator studies. It should be noted that not only the absolute calibration is important. Even if the calibration is not perfect, a comparison of lidar and model data permits a thorough comparison of vertical structures such as the thickness and heights of aerosol layers.

As a last step, the high-resolution ACL data was gridded to the model's vertical resolution as well as over 15 min by temporal averagingand to 15 min time steps. This also improved the signal-to-noise ratio of the ACL data.

3.3 Ash Transport Simulation of COSMO-ART

COSMO-ART was set up by the DWD in collaboration with Karlsruhe Institute of Technology (KIT) for an ash-dispersion simulation of the volcanic emissions during the eruptive phase of Eyjafjallajökull in spring Spring 2010 (Vogel et al., 2014). The model domain had a horizontal resolution was configured to a horizontal grid size of 7 km and 40 height layers. The height layers have a variable thickness layer thickness was variable, ranging from several meters near ground to a layer thickness of about 3 km in 22 km height above ground level. The spatial extend and model set-up is equal to the COSMO-EU domain as it is used at DWD for operational weather forecasting. A more general description of the model run is given by Vogel et al. (2014).

For this study, we used the 78-hour forecast was used, beginning at 15 April 2010, 00:00 UTC, which includes volcanic ash emission data since 14 April 2010, 06:00 UTC.

Volcanic ash was represented by six discrete size classes with a spherical shape and aerodynamic diameters of 1 µm, 3 µm, 5 µm, 10 µm, 15 µm and 30 µm. For each class, a number concentration was predicted by the model. Particles within a class were treated as equalbeing identical, i. e., they had having the same size, shape, and complex index of refraction (monodisperse classes). We therefore calculated distribution), so the calculation of effective optical cross sections as explained in follows

Section 2.2.4. The lower and upper size margins R_{d_a} and R_{d_b} were defined as ~~the arithmetic average between~~ arithmetic averages of two subsequent size classes. The lower margin of the smallest size class was half its nominal diameter~~. The~~ ; the upper margin of the largest size class was 1.5 times its nominal diameter. The resulting class ranges are shown in Fig. 3.

A list of model variables used for the forward operator is given ~~in~~ by Table 1. ~~While the p number density is taken directly from model output, the molecule number density of air was calculated from temperature and pressure according to Eq. .~~

3.4 Volcanic Ash Properties

A detailed analysis of the emitted ash was performed by Schumann et al. (2011) who compared measurements ~~made~~ from DLR's Falcon 20 aircraft with ~~the data of some German~~ data of research lidar systems ~~. Ash~~ in Germany. Eyjafjallajökull ash samples were taken in-situ, analyzed using a scanning electron microscope, and assigned to matter groups. From the matter components, the complex index of refraction was calculated.

~~Schumann et al. (2011) stated that~~ According to Schumann et al. (2011), the real part of the refractive index was between 1.53 and 1.60 at a wavelength of $\lambda = 630\,\mathrm{nm}$ and between 1.50 and 1.56 at a wavelength of $\lambda = 2000\,\mathrm{nm}$. The respective imaginary part was ranging from $-0.001\,\mathrm{i}$ to $-0.004\,\mathrm{i}$ at a wavelength of $\lambda = 630\,\mathrm{nm}$ and from $-2.0 \times 10^{-6}\,\mathrm{i}$ to $-40.0 \times 10^{-6}\,\mathrm{i}$ at a wavelength of $\lambda = 2000\,\mathrm{nm}$.

Electron microscope images from the same study revealed that the volcanic ash particles were sharp-edged with a complex and asymmetric shape. The average asymmetry factor was 1.8 for small particles ($<0.5\,\mu\mathrm{m}$) and 2.0 of larger particles (Schumann et al., 2011). Electron microscope measurements of Rocha-Lima et al. (2014) showed that the asymmetry factor of the volcanic ash fine fraction ~~has a value~~ was between 1.2 and 1.8.

The particle growth due to hygroscopic water coating was quantified to about 2 to 5 % at a relative humidity of 90 % (Lathem et al., 2011). A growth of 5 % does not change the scattering properties significantly in relation to the size averaging ~~we perform.~~

~~Nevertheless, each measurement contains an error and the ash properties may change during its travel~~ which is performed for monodisperse size classes in the forward operator. But even perfectly known volcanic ash particles will change their constitution while traveling through the atmosphere. It is therefore ~~straightforward~~ essential to analyze the maximum ~~error due to variations of the volcanic ash~~ uncertainty for applying the forward operator on volcanic ash particles with variable properties, namely the particle size, refractive index, and shape.

4 Sensitivity Studies

The representation of the particles by the model is clearly ~~simplifying, so we must study~~ simplified, so the effect of these simplifications on the scattering of laser light ~~when developing a~~ must be determined when applying the forward operator. For a lidar forward model, sensitivities of the backscatter cross section are critical because the received signal intensity is linearly coupled to the backscatter cross section and, consequently, to the attenuated backscatter coefficient.

Prior studies already showed the complexity of non-spherical scattering calculations but there is no universal solution to the problem available. Gasteiger et al. (2011b) use Discrete Dipole Approximation (DDA) to calculate the scattering properties of complex shaped particles but the analysis ~~is~~ was limited to size-parameters up to 20.8 ~~(which results in a maximum particle radius of about 3.2 µm~~ due to the increasing computational time per iteration for increasing particle sizes. The equivalent radius at a wavelength of 1064 nm ~~). A~~ would be 3.2 µm. The computation of a high-resolution multi-dimensional look-up table for up to 10 times larger particles would require unfeasible long time. The study of Kemppinen et al. (2015) ~~is~~ focused on individual ellipsoids but ~~we neither know the ellipsoidal properties nor does COSMO-ART predict changes of the volcanic ash classes. Guessing~~ assuming an ellipsoidal distribution ~~for the model predictions thus~~ to represent fractional and sharp edged particles may lead to less realistic scattering calculation results than assuming spherical scatterers. Consequently, there is no ~~sufficient~~ scattering description for Eyjafjallajökull ash predictions of COSMO-ART available. ~~We therefore~~ It is important to treat the volcanic ash as spherical objects with given optical properties (see 3.4) but analyze and discuss the effect of ~~uncertain~~ variable volcanic ash properties in the following.

It must be noted that these studies are required for ~~nearly any aerosol~~ most aerosol types as most naturally-occurrent aerosols are not perfectly spherical ~~. As we will show below, already slightly aspheric~~ and even slightly non spherical ellipsoids may have very different scattering characteristics compared to ~~perfect~~ ideal spheres.

4.1 Prerequisites

Look-up tables (LUT) of Mie efficiencies and optical cross sections have been created to reduce the effort on time-consuming scattering calculations. The look up tables have three dimensions: size parameter $X_\lambda(R_p)$, real part of the refractive index m and imaginary part of the refractive index m'.

The reasonable range of size parameters depends on the wavelength of ~~typical lidar instruments~~ the lidar transmitters and the radius of occurring particles R_p. ~~From Eq. , for~~ For the ACL systems operating at $\lambda = 1064\,\mathrm{nm}$, we find a size-parameter range of 1.18 ($R_p = 0.2\,\mu\mathrm{m}$) and 142 ($R = 24.2\,\mu\mathrm{m}$), see Eq. (10). ~~We selected a radius increment of 0.024 µm.~~

~~The~~ As explained in section 3.4, the refractive index measurements by Schumann et al. (2011) were not performed for the exact wavelength of the ACL systems~~as explained in section 3.4~~. Therefore, ~~we have to assume the refractive index we use as reference as well as an~~ the reference refractive index and the interval of uncertainty had to be assumed. Schumann et al. (2011) take a refractive index of 1.59 - 0.004i for their medium "M" case study and therefore, ~~we also used this value~~ this value is also used as reference for our study. ~~Our~~ The uncertainty intervals of real and imaginary parts were chosen according to the range of measured values at 630 nm and 2000 nm, namely a real part range of 1.54 to 1.64 and an imaginary part range of -0.006 to -0.002. To get an estimate of the overall refractive index sensitivity for such particles, ~~we decided to extend~~ the range of analyzed refractive indices was extended to real parts between 1.49 and 1.69 using increments of 0.001 and to imaginary parts between -0.011 and -0.001 using increments of 0.00005. ~~Consequently~~Using a radius increment of 0.024 µm, the total element number of one LUT is 4.0×10^7 ~~. These~~ and these look-up tables were the base for the refractive index sensitivity study.

4.2 Sensitivity to the Complex Index of Refraction

~~Fig. 4 and Fig. 5 show~~ Extinction cross section σ_{ext} and backscatter cross section σ_{bsc} as well as the effective extinction cross section $\overline{\sigma_{\mathrm{ext}}}$ and effective backscatter cross section $\overline{\sigma_{\mathrm{bsc}}}$ ~~against the~~ plotted over real and imaginary parts of the complex index of refraction ~~.~~ are shown in Fig. 4 and Fig. 5. While the extinction cross section σ_{ext} is more sensitive to the real part than to the imaginary part of the refractive index, the backscatter cross section σ_{bsc} is strongly sensitive to both. These sensitivities are strongly reduced for the effective extinction cross section $\overline{\sigma_{\mathrm{ext}}}$ and the effective backscatter cross section $\overline{\sigma_{\mathrm{bsc}}}$.

~~An overview of~~ A measure for the refractive index sensitivity of the effective optical cross sections is given by Fig. 6 which shows the relative errors

$$\sigma_{\mathrm{ext,err},p}(m,m') = \frac{\overline{\sigma_{\mathrm{ext},p}(m,m')} - \overline{\sigma_{\mathrm{ext},p}(m^*,m'^*)}}{\overline{\sigma_{\mathrm{ext},p}(m^*,m'^*)}} \cdot 100\%, \tag{24}$$

and

$$\sigma_{\mathrm{bsc,err},p}(m,m') = \frac{\overline{\sigma_{\mathrm{bsc},p}(m,m')} - \overline{\sigma_{\mathrm{bsc},p}(m^*,m'^*)}}{\overline{\sigma_{\mathrm{bsc},p}(m^*,m'^*)}} \cdot 100\%. \tag{25}$$

~~The relative error is~~

It is defined as the error of the optical cross sections if ~~we assume that the refractive index we defined as reference~~ the reference refractive index (m^* and m'^*) was assumed to be true but the real particles have a refractive index of m and m'. ~~We can conclude~~ It can be concluded from this analysis that the maximum relative error for the given range of refractive indices is less than 10 % for the extinction cross section but ranges up to 230% for the backscatter cross section at the outer extremes of the uncertainty range.

4.3 T-matrix Particle Shape Sensitivity Study

T-matrix calculations ~~within~~ performed in this study are based on the FORTRAN code for randomly oriented particles, written and provided by Mishchenko and Travis (1998). A detailed description of the method can be found in ~~the work of~~ Mishchenko et al. (2002).

~~We modified the~~ The double-precision version of the T-matrix procedure was modified to perform scattering calculations of multiple particle sizes automatically. In addition to that, the procedure was extended by ~~the calculation of the~~ calculating and returning the backscatter cross section σ_{bsc} according to Mishchenko et al. (2002), Eq. (9.10). ~~Then, as a test, both mie_single and our modified T-matrix code were set up to calculate the scattering properties of the same spheres and for the same wavelength. The results of both procedures were indeed~~ These modifications were tested by comparing the scattering calculation results of the modified code and mie_single for spherical particles and the results were identical.

A list of T-matrix options we used for the particle shape sensitivity study is ~~shown in~~ Table 2. The most important particle properties are defined by the variables NP and EPS. NP ~~defines~~ is the particle type descriptor and has a value of -1 for spheres as well as for ellipsoids. A NP value of -2 is used for cylinders. The variable EPS is an expression for the objects' diameter to

length ratio~~. Consequently, an~~ : An ellipsoid with EPS=1 is a sphere, prolate objects have ~~an~~ EPS<1 and oblate objects have ~~an~~ EPS>1.

In Figs 7, 8, and 9, the optical cross sections and the pure lidar ratio of spheres and several aspherical particles are plotted against the equal-volume radius. The aspherical scatterers are 6 ellipsoids with a diameter-to-length-ratio of 0.50, 0.67, 0.75, 1.25, 1.50 and 2.00 as well as 5 types of cylindric particles with a diameter-to-length-ratio of 0.50, 0.80, 1.00, 1.25 and 2.00. ~~As shown in these plots, the results for~~ Unfortunately, the scattering properties of a highly asymmetric ellipsoid (EPS: 0.50) is only available up to an equal-volume radius of 3.75 µm. For future research activities in this topic, the quadruple precision version of the t-matrix code ~~should be preferably used~~ could be used to extend the upper size range of highly asymmetric particles.

~~We found no significant differences of~~ No significant differences between the extinction cross section of spheres and these ellipsoids were observable. By trend, however, cylindric shaped particles have a higher extinction cross section compared to ellipsoids~~and the spherical shape has the~~ . Spheres have the lowest extinction cross section values over the whole spectrum. Up to a volume-equivalent radius of 0.7 µm, the shape effect is not noticeable.

Regarding the backscatter cross section, ~~however, we find~~ there are significant differences between the backscatter cross section of spheres and particles with other shapes. Obviously, spheres are affected by interference effects which lead to both fluctuating and oscillating values of the backscatter cross section while the ~~other shapes only show weakly fluctuatingvalues of the backscatter cross section~~backscatter cross section spectrum of other shapes is only weakly fluctuating. As observed for the extinction cross section, the shape effect becomes pronounced beginning at an equal-volume radius greater than 0.7 µm. Spherical scatterers have a higher value of the backscatter cross section compared to ellipsoids except for one type of ellipsoid (EPS = 1.25). For cylinders, ~~such interference effects are not observable so~~ the backscatter cross section of the ~~considered cylinders~~ analyzed aspect ratios increases monotonically with ~~the equal-volume radius~~size. As a result, the backscatter cross section of spheres is lower than of cylindric particles with the same size if their equal-volume radius is greater than 3.75 µm (for the given wavelength of $\lambda = 1064\,\mathrm{nm}$).

The particle shape effect on the pure lidar ratio is ~~only~~ weakly pronounced for small particle sizes (less than 0.75 µm)~~, too~~. For larger particles, the pure lidar ratio of spheres is generally lower than of the other considered shapes which is in agreement to the higher backscatter cross section observed before. For the fourth size class (equal-volume radii around 5 µm), the previously observed interference effects of the spheres' backscatter cross section leads to extreme values of the pure lidar ratio (exceeding a ~~lidar ratio~~ value of 200 sr). ~~By trend,~~ For the size classes 2, 3 and 5, however, the pure lidar ratio of spheres ~~in this size class is not that different than the lidar ratio of other considered shapes. But for the other size classes, the lidar ratio of spheres is the lowest of all observations except for cylinders which have a lidar ratio value at the same order of magnitude as spheres~~is lower than of all other considered particle shapes except for cylinders. This indicates that the assumption of spherical scatterers results in an underestimation of the total lidar ratio if the considered particles are not spherical and size classes 2, 3, and 5 contribute predominately to the total volcanic ash number density.

A summary of the particle shape sensitivity study is shown in Figs 10 ~~, 11, and ??,~~ and 11, giving the relative differences of the effective optical cross sections ~~and average lidar ratios~~ for different particle shapes. The definition of the relative differences

follows Eq. (24) and Eq. (25). ~~Again, the reference is a spherical particle. Positive and negative relative differences indicate that the calculated values for spheres are underestimations and overestimations compared to respective non-spherical particles.~~

The effective extinction cross section of spheres is ~~lower~~ smaller than the effective extinction cross section of other analyzed asymmetric particles. Regarding the effective backscatter cross section, however, ~~we find relative differences of up to~~ the maximum relative differences are 300% and −80%. While the small aspherical particles have a ~~lower~~ smaller effective backscatter cross section compared to spheres, the effective values of the fourth size class are higher ~~for~~ compared to almost all considered aspherical particles. From this analysis, it can be concluded that due to the assumption of sphericity, the backscatter cross section of size classes 1, 2 and 3 are overestimated by about factor 1.5 to 5 while the backscatter cross section of the fourth size class is underestimated by factor 2. This allows for quantifying the over- and underestimation of the results for each size class individually which is not possible for forward operators ~~where~~ based on assuming a fixed lidar ratio~~is assumed~~.

~~The relative difference of the average lidar ratio shows that assuming spheres for the scattering calculations results in much lower lidar ratio values of size classes 2 and 3 but in higher lidar ratio values than would be observed for a mixture of particle shapes. For the fourth size class, the opposite has been observed: assuming spheres leads to an higher values of the lidar ratio of large particles than for non spherical particles of the same size. The lidar ratio of the first class, however, is nearby independent on the particle shape.~~

~~Of course, the total effect of different particle shapes for a real aerosol mixture has to be estimated with more extensive scattering calculations. For the current state of the forward operator research, the spherical shape has to be used as reference even if the real volcanic ash particles are known to be fractal and complex shaped. One of the reasons for doing so is the fact that there is currently no appropriate shape representation scheme for volcanic ash available. For example from the findings of Rocha-Lima et al. (2014), the average aspect ratio of volcanic ash is known but not a representative particle shape. As we have shown, the backscatter cross section of cylinders also differs tremendously from ellipsoids and from spheres etc. so there is currently a lot of indication that using a given aspherical shape as reference would yield in even higher errors than assuming a spherical shape.~~

~~The above results, however, give us valuable insight into the uncertainties of using Mie calculations for non-spherical particles. These findings are important for interpreting the results of the forward operator.~~

5 ~~Results~~Comparison of Model Output with Observations

5.1 Scattering Properties of Volcanic Ash Used Within the Forward Operator

A list of ~~the~~ effective extinction cross section and ~~the~~ effective backscatter cross section ~~we determined~~ values for atmospheric gas molecules and for the six volcanic ash size classes is shown in Table 3.

5.2 Output Variables of the Forward Operator

Using the forward operator allows for plotting each variable of the lidar simulation for analytic purposes (see Fig. 12). These plots of forward-operator output variables are representing the major characteristics of the variables: strong extinction and strong backscattering are usually related. Time and height intervals ~~at which~~ where only molecules exist, lead to low values of the extinction coefficient and backscatter coefficient. Due to the decrease of the atmospheric gas number density with height, both extinction and backscatter coefficient decrease with height in an aerosol-free atmosphere. The two-way transmission decreases with height (see Eq. (19)).

In ~~addition, the volcanic ash~~ comparison with Raman lidar measurements, both the maximum measured extinction coefficient of $4.0 \times 10^{-4}\,\mathrm{m}^{-1}$ and the maximum backscatter coefficient of $8.0 \times 10^{-6}\,\mathrm{m}^{-1}\,\mathrm{sr}^{-1}$ inside the volcanic ash plume (Ansmann et al., 2010) nearby equal to the respective maximum values output by the forward operator at the station Deuselbach: The Raman lidar measured values are slightly lower than the values output by the forward operator which could be due to assumptions related to the forward operator or due to an over-estimation of the COSMO-ART predicted aerosol number density.

From output of the forward operator, the relative contribution to the total signal and to the total mass density ~~was~~ can be analyzed for each size class of COSMO-ART ~~within two case studies. The cases were selected to cover extreme situations: Case 1 is the~~ and also the total lidar ratio can be calculated. This was done exemplary at two time-height coordinates: The first coordinate points to model output from a coordinate inside the volcanic ash layer (Table 4). ~~Case~~ Coordinate 2 ~~is for~~ points to a coordinate where the ~~majority of particles are due to size class~~ major fraction of the particle mass is contributed by size classes 4 and 6 (see Table 5).

Regarding ~~case~~ coordinate 1, the total backscatter coefficient is dominated by ash size classes 1, 2 and 3 while the signal contribution of classes 4 to 6 is less than 5 % in total. The mass contribution is dominated by classes 3 and 4 while classes 2, 5 and 6 are contributing by 10 % each to the total mass density~~and class 1 is very low for the total mass density. Regarding case~~. The total lidar ratio is 9.63 sr. Regarding coordinate 2, the total backscatter coefficient depends by about 68 % from class 4 and by 30 % from class 6. The mass contribution in ~~case~~ coordinate 2 is also dominated by the classes 4 and 6 but, in contrast to the backscatter coefficient, class 6 has a higher contribution to the total mass density than class 4. The total lidar ratio at this coordinate with predominately large particles is 46.53 sr.

General conclusions from this analysis about the relationship between backscattering and mass, depending on particle size and wavelength, require further investigation. For ~~our~~ an application of the forward operator in this study, however, ~~we can conclude the following~~there are two aspects to be mentioned: First, the ~~total signal~~ backscattering intensity inside the volcanic ash layer (~~case~~ coordinate 1) is ~~predominately~~ predominantly dependent on classes 1, 2 and 3 whose backscatter cross sections are also overestimated by the forward operator due to the assumption of sphericity (see Fig. 11). The real values of the ~~attenuated backscatter coefficient~~ total lidar ratio may be by factor 2-3 higher ~~.~~ in certain cases (see Sect. 4.3). Second, the larger particles of classes 4, 5 and 6 carry a large portion of the mass but contribute only weakly to the total signal. This may be ~~an~~ important information for the selection of future ACL networks~~as~~. Prior studies confirm that even the systems operating

at a relatively long wavelength of 1064 nm have a reduced sensitivity for ~~particles within these size classes~~giant and ultragiant particles (Madonna et al., 2013).

5.3 Qualitative Comparison

A ~~qualitative comparison allows for the identification of common and different structures between the measured and simulated lidar profiles. Different ash layer structures can hint, e.g., to errors in the model dynamics, in the source description, or in the sedimentation parametrization. If ash structures are found only in the measured profiles, either the model prediction is wrong or it misses an important aerosol type which is not present in the model. If structures are visible in the forward modeled profiles but missing in the measured profiles, either the ACL signal is too weak because of high extinction in lower heights or the model performed a wrong ash prediction. But it is also possible that the model overestimates the ash concentration so the structures are below the detection limit of the ACL measurements.~~

~~For a qualitative comparison between measurement and simulation, we chose~~ comparison of ACL measurement and COSMO-ART simulation with an applied forward operator at the ACL station Deuselbach in West Germany ~~and a time interval from 16 to 17 April 2010 as an example. Here, the~~ is shown in Fig. 13. The ash layer was clearly visible in the measured profiles without being affected by low-level or high-level clouds. ~~We calculated the attenuated backscatter coefficient from the ACL measurement according to Eq. , extracted the common time and height intervals and re-sampled the ACL data to the model resolution.~~

~~A comparison of ACL measurement and COSMO-ART simulation with an applied forward operator is shown in Fig. 13.~~ Due to the inevitable instrumental noise, the automatic calibration of ACL system and subsequent background subtraction, some data points become negative which is just a statistical effect but causes missing data in the log-scale plots. Volcanic ash plumes are clearly visible on both plots. Looking at the forward operator result, the ash layer begins to cross the ACL station between 06:00 UTC and 12:00 UTC at 16 April 2010. The layer height decreases with time and partially entrains into the planetary boundary layer where it persists even at the end of 17 April 2010. As both model and forward operator only represent volcanic ash and air molecules, the ash layers can be tracked within the planetary boundary layer. This is not possible using ACL measurements alone as the volcanic ash signal is tainted by other aerosol types~~here~~. It is, however, ~~rather~~ difficult to determine unambiguously which ash layer structure observed by the ACL instrument can be related to the appropriate structures simulated by the model. Regarding the thin volcanic ash layer which is measured by the ACL instrument in a height between 7 and 9 km ASL at ~~the~~ 16 April 2010, around 06:00 UTC, this feature could be equivalent to the model prediction of ash in a height of 6 km ASL at 7:00 UTC. In this case, the model would have performed a rather precise prediction with only one hour time lag and a two km vertical shift. But it is also possible that the predicted ash entrainment over the ACL station is equivalent to the ash-indicating ACL signals at around 12:00 UTC. In the latter case, the model prediction would be wrong by a time lag of about 6 hours which is insufficient for time-critical applications.

The qualitative comparison is currently limited to coordinates where the major fraction of scatterers are represented by both model and forward operator. There ~~is~~are, however, ~~one scatterer fraction~~ some scatterer fractions still missing on the present model runs for a comprehensive comparison: Other aerosol types than volcanic ash like anthropogenic emissions, mineral dust, soot, pollen, etc., are not included which leads to differences especially in the planetary boundary layer. ~~We therefore~~

~~cannot~~ It is hard to predict yet whether the strong ACL signal in the planetary boundary layer is related to background aerosol extinction or errors of the ~~model~~COSMO-ART prediction. To further investigate this problem, future studies with several types of aerosols incorporated into the model ~~will be helpful~~are required.

5.4 Quantitative comparison

A major purpose of the backscatter lidar forward operator is the capability to perform also quantitative comparisons of measurement and model output data. Unfortunately, such comparison is of limited validity in this case study due to the unknown ACL calibration as noted in Section 3.2.

Outside the volcanic ash layer, the forward operator returns ~~an~~ attenuated backscatter coefficient values of $1 \times 10^{-7}\,\mathrm{m^{-1}\,sr^{-1}}$ which is equal to the values of the ACL instrument after calibration. This would be expected as both temperature and pressure are rather precisely determinable and the scattering properties of air are represented by the empirical equations which are used for the forward operator. ~~We therefore assume that~~ Thus, the selected calibration factor ~~is~~ seems to be valid for this scenario.

Regarding the attenuated backscatter coefficient inside the ash layer, however, the forward operator returns stronger signals inside the ash plume as well as a lower transmission behind the ~~cloud~~ ash plume compared to the ACL measurement. The maximum ~~values~~ value of the attenuated backscatter coefficient returned by the forward operator (about $6.0 \times 10^{-4}\,\mathrm{m^{-1}\,sr^{-1}}$) is ~~60~~ 20 times higher than the maximum ~~values~~ value reported by the ACL (about $3.0 \times 10^{-5}\,\mathrm{m^{-1}\,sr^{-1}}$). ~~The minimum attenuated backscatter coefficients calculated by the forward operator ($1.0 \times 10^{-9}\,\mathrm{m^{-1}\,sr^{-1}}$) are about 10 times lower than observable on the ACL plots ($1.0 \times 10^{-8}\,\mathrm{m^{-1}\,sr^{-1}}$), excepting pixels which became negative due to noise. Above the cloud (~~Also, the forward modeled attenuated backscatter coefficient shows strong attenuation due to the volcanic ash layer in about 12 km ASL~~), ;~~ the attenuated backscatter coefficient is by about factor 10-15 lower than in ~~the same height but without passing through the volcanic~~ same heights above clean-air situations. Both findings indicate an over-estimation of the model-predicted volcanic ash number-density. In the case of determining the hazardousness of volcanic ash particles using ash dispersion models, however, an over-estimation of the ash ~~. The two-way transmission at this height is thus about 7-10 % which seems to be a too low value compared with the observations.~~ concentration and preferring false alarms over misses are reasonable strategies.

~~We therefore analyzed the effect on the attenuated backscatter coefficient if the model-predicted ash number densities are being reduced by factors of 10, 20 and 30. If the ash number density is reduced by factor of 20 (Fig. **??**), similar maximum values of the attenuated backscatter coefficient are observed inside the ash layer for both the forward operator and the ACL ($5.0 \times 10^{-5}\,\mathrm{m^{-1}\,sr^{-1}}$). This reduction of the number density also results in less extinction, and the two-way transmission has a minimum value of 70 % (plot not shown here) which is more realistic than the minimum value observed for the original dataset (8 %, see Fig. 12).~~

6 Conclusions

A backscatter lidar model capable of calculating both the extinction and backscatter coefficients was introduced. Detailed studies concerning the scattering properties of particles and molecules were performed. Instead of assuming a lidar ratio for given particles, this forward operator allows for calculating the scattering properties even for mixtures of different particle types. ~~The shown method allows for an efficient calculation of ACL profiles based on the output of atmospheric chemistry models.~~

~~The forward model was applied to the COSMO-ART model but the same approach can be used for any other aerosol-chemistry-transport model.~~ Data of a COSMO-ART ash-dispersion simulation for the Eyjafjallajökull eruption in 2010 was used to run the forward operator and perform both qualitative and quantitative comparison between the output of the forward operator and measurement data of an automated ceilometer lidar (ACL) system.

A major challenge for setting up the forward operator ~~in~~ for a given scenario are ~~the~~ scattering calculations, namely the calculation of the effective extinction cross section $\overline{\sigma_{\mathrm{ext},R_d,k,\lambda}}$ and the effective differential backscatter cross section $\overline{\sigma_{\mathrm{bsc},R_d,k,\lambda}}$ of all model-represented particle size and type classes.

The atmospheric gas mixture ~~could be simplified to~~ was treated as a uniform mixture of ~~"atmospheric gas". Therefore, empirically determined scattering equations~~ *atmospheric gas* and empirical scattering formulas were used to calculate ~~the~~ its optical cross sections ~~of this mixture for the given~~ for the ACL laser wavelength. From the model-predicted values of temperature and pressure, the molecule number-density and finally the molecule extinction and backscatter coefficients were calculated.

For particle scattering, ~~extensive scattering calculations are the basis for look-up tables of optical cross sections. The~~ the range of particle sizes was selected according to the volcanic ash ~~size~~ classes used by COSMO-ART (six monodisperse classes with diameters of 1 µm, 3 µm, 5 µm, 10 µm, 15 µm and 30 µm). The range of considered refractive indices were adapted according to in-situ measurements of Schumann et al. (2011).

Due to uncertain refractive indices and shapes of the volcanic ash~~and the fact that volcanic ash particles show complex shapes~~, sensitivity studies have been performed to analyze the impact of different particle types and shapes on the effective extinction and backscatter cross section ~~as well the~~ and the pure lidar ratio. While the extinction cross section was only weakly sensitive to variable refractive indices and particle shapes, the backscatter cross section was strongly sensitive to both. However, ~~we found that~~ the sensitivities reduce significantly, when ~~averages over size classes are made. We expect that this very interesting result - described in this manuscript for the first time - will be very helpful for comparisons of modeled with measured backscatter lidar data.~~

~~Using these effective optical cross sections reduced the sensitivity of optical cross sections regarding the refractive index as well as the particle shape. But even after~~ applying size-averaging algorithms. After averaging, the relative uncertainty of the effective backscatter cross section ~~exceeds~~ is up to 280% ~~for uncertain~~ within the defined range of refractive indices. This study also indicates the dependency of the forward operator on precise information about the particle's refractive index. ~~Within~~

~~a particle shape sensitivity study, we were able to resolve the relative uncertainty of each individual size class for the effective backscatter cross section. Assuming that volcanic ash consists of a mixture~~

From the findings of Rocha-Lima et al. (2014), the average aspect ratio of volcanic ash is known but there is no information about a distribution function of particle shapes ~~, we analyzed the relative differences between the reference particle shape and~~ and real volcanic ash particles have an infinite variety of particle shapes. In consequence, the spherical shape was used as reference even if the real volcanic ash particles are known to be fractal and complex shaped. Within a particle shape sensitivity study, the impact of the particle shape on extinction and backscatter cross sections was analyzed for 11 particle shapes (6 types of ellipsoids and 5 types of cylinders).

~~The forward operator matches the~~ The backscatter cross section spectrum of cylinders was different than the spectrum of ellipsoids and spheres. Sensitivity studies as presented here are mandatory for stepwise improving the knowledge in scattering calculations related to lidar forward models. More detailed studies of scattering at non-spherical particles are thus mandatory to better represent the particle shape in the calculation of the effective backscatter cross section.

In literature, we find measured lidar ratio values ~~we find in literature (40 sr to values higher than 100 srfor volcanic ash (Kokkalis et al., 2013; Ansmann et al., 2010; Mortier et al., 2013)). On average, the~~ for volcanic ash between 40 sr and values greater than 100 sr, (Kokkalis et al., 2013; Mortier et al., 2013). This range of values could be observed within sensitivity studies of the pure lidar ratio (Sect. 4.3). From our analysis, the assumption of spherical particles results in a general under-estimation of the lidar ratio except for size classes 1 and 4. Comparing the pure lidar ratio ~~is 61.17 sr which fits well to the literature findings. Comparing the lidar ratio~~ values of the first two size classes with the ~~lidar ratio~~ values reported by Gasteiger et al. (2011b), ~~a lidar ratio~~ values of less than 20 sr ~~seems~~ seem to be plausible for these ~~particle size to wavelength ratios~~size parameters. The authors found even for irregularly shaped objects a pure lidar ratio between 5 sr and 20 sr at size parameters between 5 and 15 (equivalent particle diameter at $\lambda = 1064\,\mathrm{nm}$ ~~would be~~ is 1.6 µm and 4.8 µm, respectively). ~~We therefore assume that the calculation results of the backscatter lidar~~ The pure lidar ratio values output by the forward operator are ~~valid and allow for both qualitative and quantitative comparison.~~ thus realistic.

The total lidar ratio calculated at two sample coordinates of COMSO-ART output resulted in values of 9.63 sr and 46.53 sr, respectively, which is - for the first coordinate - lower than the lidar ratio values of the Eyjafjallajökull ash plume measured by Raman lidar at Munich and Leipzig. From our analysis of the pure lidar ratio, we found an under-estimation of the calculated lidar ratio for some size classes due to the assumption of spherical volcanic ash particles. However, the particle size class configuration of the model could also have a huge effect on the calculated lidar ratio values due to the ash size coverage and ash size class width configuration. Therefore, the forward modeled total lidar ratio in this scenario is not expected to match the lidar ratio derived from measurements exactly. Further investigation in this topic is required to optimize the particle size class configuration of models using monodisperse size classes and the representation of non spherical particles in the forward operator towards a better representation of the total lidar ratio.

A ~~comparison between~~ time-height cross section comparison of ACL measurement and ~~the model predictions used as input for the developed forward operator~~ forward modeled COSMO-ART output was shown. Similar structures were observed but some features were referenced to different ~~time and height locations. From our~~ times and heights. From the analysis at the ACL

station Deuselbach, some ash layer features were predicted quite precisely by the model, for example the time of arrival of the ash plume at about 06:00 UTC ~~with a vertical shift of~~ but vertically shifted by about 1.5 km. ~~Some other features, such as the~~ The ash plume intersection with the planetary boundary layer at 17 April 2010, 03:00 UTC ~~,~~ was simulated about 6 hours too early ~~to~~ at 16 April 2010, 18:00 UTC. Fine structures of the ash layer were only observable in the simulation but not in the ACL ~~measurements~~ data due to noise. Furthermore, the contribution of individual classes to the total backscatter coefficient and to the total mass density for two sample cases were analyzed.

~~Due to unknown~~ The missing calibration coefficients of the ACL system, required to define a calibration constant η^* ~~was estimated by~~ and estimate its value comparing the ACL data with calibrated measurements at the same wavelength. Within quantitative comparisons between ACL measurements and the forward operator output, ~~we found that~~ the molecule signal of ACL and forward operator output were ~~of~~ in the same order of magnitude which argues that the selected calibration factor was reasonable. ~~Meanwhile, the ACL manufacturers have understood the importance of calibrated backscatter data and implemented technical solutions so that a similar effort as described in this study with data for the year 2010 became obsolete.~~

A comparison ~~the volcanic ash signal~~ of the measured and forward modeled volcanic ash attenuated backscatter coefficient inside the volcanic ash plume led to the conclusion that the model predicted ash concentration was ~~to be too high as the forward modeled attenuated backscatter coefficient within ash layers was 60 times higher and after attenuation 10 times lower than observed by the ACL. If the~~ too high which could be potentially resolved by reducing the model-predicted ash concentration ~~is manually reduced by a factor of 20,~~ manually by a given factor until the forward modeled COSMO-ART predictions and ACL measurements ~~became~~ are quantitatively similar. Such a reduction could be part of a simple particle data assimilation system helping to calibrate particle dispersion simulations before in-situ measurements are available - assuming that the particles optical properties are known. It is therefore required to develop methods in the future which allow for a fast determination of an aerosol type's refractive index range, shape- and aspect ratio description. ~~It would of course be beneficial, if even better information on the refractive index and effective particle shape and aspect ratio of volcanic ash particles becomes available in the future.~~

~~Furthermore, we analyzed the contribution of each class to the total backscatter coefficient and to the total mass density for two sample cases. Regarding case 1 inside the volcanic ash layer, the classes 1, 2 and 3 were mostly responsible (94.8 %) for the calculated attenuated backscatter coefficient. As these classes contribute most to the forward modeled signal, the value of the lidar ratio would also be expected to be dominated by their contribution, namely a value between 5.23 sr and 58.83 sr (see Table 3). Raman lidar measurements of the Eyjafjallajökull ash resulted lidar ratio values greater than about 40 sr at wavelengths of 355 nmand 532 nm (Großet al., 2012) which is within this range. Thus, the calculated values of both extinction and backscatter cross section as well as the lidarratio seem to be plausible.~~ As aerosol dispersion processes are directly coupled to vertical and horizontal movements in the atmosphere, a comparison of forward modeled and measured backscatter lidar profiles offers great potential for validating and improving the dynamic and thermodynamic components of an atmospheric chemistry model. For a model with variational data assimilation methods, the data assimilation system would select the prediction variation which fits best to the atmospheric state provided by lidar measurements, resulting in a continuous adaptation of the model prediction to the real world situation.

~~Assuming that the ACL calibration is valid, the model-predicted ash concentration was about 10 times higher than observable.~~ The absolute values reported by the Raman lidar systems at a wavelength of 1064 nm, however, agreed within the measurement uncertainties and expected natural differences in the sampled air mass with the results of the forward operator, see Sect. 5.2. This is quite remarkable given the large uncertainties of the ash data in the model (assumed emission rate of the volcano, atmospheric dynamics, dynamic of the modeled ash plume in the atmosphere including sedimentation), and that there is no data assimilation regarding aerosol data at all yet. Further studies could focus on comparison between forward modeled lidar profiles and measurements from Raman or multi-wavelength lidar. In this context also the upcoming ESA satellite sensor EarthCARE with its high-spectral resolution lidar is certainly of high interest.

There are, however, some error sources remaining which are: First, there are only molecules and the six volcanic ash classes represented while background aerosol is missing completely. Second, the ACL calibration is of limited precision. Third, the contribution to the attenuated backscatter coefficient of ash size classes 4, 5 and 6 is relatively low even though these classes carry a large proportion of the mass. This relationship could rely on the ACL's wavelength which probably limits its sensitivity to particles larger than about 10 µm in diameter. Such results strengthen the importance of a joint use of observations and model output in combination with data assimilation in order to get ~~the best state of the atmosphere~~ a reliable description of the atmospheric state with respect to aerosol distributions and properties.

Conclusively, ~~we recommend~~ further investigation in scattering calculations of non-spherical particles is recommended to get more realistic optical cross sections for the forward operator. A decrease of uncertainties related to the forward operator can be achieved by refractive index measurements at the exact ACL wavelength. Refractive index measurements are a basic aspect of the forward operator as the optical cross sections can only be calculated if the aerosols' refractive index is known precisely. The model - and consequently the forward operator - ~~has to~~ must represent more aerosol types, especially background aerosols, mineral dust, sea salt and soot as missing extinction near ground may cause the forward operator to overestimate the ~~signal~~ attenuated backscatter coefficient value from layers behind. But also qualitatively, more scatterer size classes are required to also represent the fine fraction and very large particles in the atmosphere. One approach for a better representation of the natural size-spectrum of aerosols is the use of continuous number-size distributions which are aggregated from multiple distribution functions ("modal" approach). On the one hand, this already includes the size-averaging which is necessary for monodisperse size distributions. But on the other hand, the model delivers exact information about the outer margins, i.e. the number-density of the fine and the extreme coarse fraction which is currently not reproduced by model and forward operator in the ~~Eyjafjallajökull~~ selected case study.

~~In the context of international and probably intercontinental ACL networks, the creation of a scattering database for aerosols would be desirable. A central database can increase the development rate and flexibility of current lidar forward operator implementations. The ACL networks themselves are only useful for aerosol research and data assimilation if the~~ As many ACL devices are operating a proprietary firmware, the manufacturers have to be sensitized to data quality and reproducible measurement calibration. Therefore, it is required that calibration is performed automatically and transparent. ~~For~~ In future lidar measurement networks, the number of high spectral resolution lidar (HSRL) systems and Raman lidar systems could potentially increase and allow for the assimilation of ~~the~~ extinction coefficient and ~~the~~ backscatter coefficient directly.

~~As many ACL devices are operating a proprietary firmware, the manufacturers have to be sensitized to data quality and reproducible measurement calibration. Otherwise, the backscatter data is nearby useless for any quantitative comparison or aerosol data assimilation approach.~~ But also for present automated lidar systems, activities are ongoing to collect, homogenize, and distribute observations in an international framework. Observation projects such as EARLINET (Pappalardo et al., 2014) and E-PROFILE (EUMETNET Profiling Programme) also focus on data quality improvements to meet the requirements of Numerical Weather Prediction (NWP). In the spirit of these international activities, the creation of a central database for aerosol scattering properties and forward operators would be desirable. Such database can increase the development rate, flexibility and applicability of current and future lidar forward operator implementations. Our operator is the basis also for other, more sophisticated operators and probably the best for backscatter lidar. The methodology and analysis presented here will be helpful for stepwise improving our knowledge in how to deal with the the important task of aerosol monitoring, modeling, and data assimilation in the future.

The uncertainties in both modeling and measurements, ~~however, will also~~ will require sophisticated data assimilation algorithms not only for typical atmospheric variables but also for aerosol optical properties. Also a very good first guess of model simulations with respect to aerosol particles will be necessary so that more sources, types, and sinks will be to be included. Within its priority project KENDA (Kilometer-Scale Ensemble Data Assimilation) the COSMO Consortium has developed an Ensemble Kalman Filter for data assimilation on the convective scale. It was scheduled for introduction into operational use by MeteoSwiss and DWD in 2016. An advantage of the ensemble data assimilation system is that the assimilation can be carried out based on the pure forward operator, and that it is not necessary to calculate derivatives of the forward operator or the adjoint tangential model for carrying out data assimilation. Also, it naturally introduces model increments for all variables where some dynamic covariance is observed from the underlying ensemble model runs. DWD aims to test the assimilation of ACL data into the COSMO-ART model based on BaLiFOp.

Acknowledgements. The present study was part of the research project 50.0356/2012 funded by the German Federal Ministry of Transport and Digital Infrastructure (BMVI, prior BMVBS). We furthermore acknowledge the contributors to COSMO-ART, to the ceilometer network, to the IDL procedure mie_single and to the T-matrix codes we used as a basis for our study. We are also thankful for helpful discussions with Cristina Charlton-Perez, Werner Thomas, and Frank Wagner. Furthermore, we like to acknowledge the travel support and very interesting discussions within the frame of the European COST ("Cooperation in Science and Technology") action "Towards operational ground based profiling with ceilometers, Doppler lidars and microwave radiometers for improving weather forecasts (TOPROF)".

References

Álvaro M. Valdebenito B, Pal, S., Behrendt, A., Wulfmeyer, V., and Lammel, G.: A novel approach for the characterisation of transport and optical properties of aerosol particles near sources – Part II: Microphysics–chemistry-transport model development and application, Atmospheric Environment, 45, 2981 – 2990, doi:http://dx.doi.org/10.1016/j.atmosenv.2010.09.004, http://www.sciencedirect.com/science/article/pii/S1352231010007582, 2011.

Ansmann, A., Tesche, M., Groß, S., Freudenthaler, V., Seifert, P., Hiebsch, A., Schmidt, J., Wandinger, U., Mattis, I., Müller, D., and Wiegner, M.: The 16 April 2010 major volcanic ash plume over central Europe: EARLINET lidar and AERONET photometer observations at Leipzig and Munich, Germany, Geophysical Research Letters, 37, n/a–n/a, doi:10.1029/2010GL043809, http://dx.doi.org/10.1029/2010GL043809, l13810, 2010.

Bangert, M., Nenes, A., Vogel, B., Vogel, H., Barahona, D., Karydis, V. A., Kumar, P., Kottmeier, C., and Blahak, U.: Saharan dust event impacts on cloud formation and radiation over Western Europe, Atmospheric Chemistry and Physics, 12, 4045–4063, doi:10.5194/acp-12-4045-2012, http://www.atmos-chem-phys.net/12/4045/2012/, 2012.

Banta, R. M., Brewer, W. A., Sandberg, S. P., and Hardesty, R. M.: Doppler Lidar–Based Wind-Profile Measurement System for Offshore Wind-Energy and Other Marine Boundary Layer Applications, American Meteorological Society, 51, 327–349, http://journals.ametsoc.org/doi/abs/10.1175/JAMC-D-11-040.1, 2012.

Behrendt, A., Nakamura, T., Onishi, M., Baumgart, R., and Tsuda, T.: Combined Raman lidar for the measurement of atmospheric temperature, water vapor, particle extinction coefficient, and particle backscatter coefficient, Appl. Opt., 41, 7657–7666, doi:10.1364/AO.41.007657, http://ao.osa.org/abstract.cfm?URI=ao-41-36-7657, 2002.

Behrendt, A., Pal, S., Wulfmeyer, V., Álvaro M. Valdebenito B., and Lammel, G.: A novel approach for the characterization of transport and optical properties of aerosol particles near sources – Part I: Measurement of particle backscatter coefficient maps with a scanning UV lidar, Atmospheric Environment, 45, 2795 – 2802, doi:http://dx.doi.org/10.1016/j.atmosenv.2011.02.061, http://www.sciencedirect.com/science/article/pii/S1352231011002056, 2011.

Benedetti, A. e. a.: Aerosol analysis and forecast in the European Centre for Medium-Range Weather Forecasts Integrated Forecast System: 2. Data assimilation, J. Geophys. Res., 114, doi:10.1029/2008JD011115, 2009.

Buchholtz, A.: Rayleigh-scattering calculations for the terrestrial atmosphere, Optical Society of America, 34, 2765–2773, 1995.

Chaboureau, J.-P., Richard, E., Pinty, J.-P., Flamant, C., Di Girolamo, P., Kiemle, C., Behrendt, A., Chepfer, H., Chiriaco, M., and Wulfmeyer, V.: Long-range transport of Saharan dust and its radiative impact on precipitation forecast: a case study during the Convective and Orographically-induced Precipitation Study (COPS), Quarterly Journal of the Royal Meteorological Society, 137, 236–251, doi:10.1002/qj.719, http://dx.doi.org/10.1002/qj.719, 2011.

Charlton-Perez, C. L., Cox, O., Ballard, S. P., and Klugmann, D.: A Forward model for atmospheric backscatter due to aerosols, clouds and rain, in: EMS Annual Meeting Abstracts, vol. 10 of *EMS2013-313*, 2013.

Chen, S., Zhao, C., Qian, Y., Leung, L. R., Huang, J., Huang, Z., Bi, J., Zhang, W., Shi, J., Yang, L., Li, D., and Li, J.: Regional modeling of dust mass balance and radiative forcing over East Asia using WRF-Chem, Aeolian Research, 15, 15 – 30, doi:http://dx.doi.org/10.1016/j.aeolia.2014.02.001, http://www.sciencedirect.com/science/article/pii/S1875963714000056, 2014.

Cuevas, E., Camino, C., Benedetti, A., Basart, S., Terradellas, E., Baldasano, J. M., Morcrette, J. J., Marticorena, B., Goloub, P., Mortier, A., Berjón, A., Hernández, Y., Gil-Ojeda, M., and Schulz, M.: The MACC-II 2007–2008 reanalysis: atmospheric dust evaluation and

characterization over northern Africa and the Middle East, Atmospheric Chemistry and Physics, 15, 3991–4024, doi:10.5194/acp-15-3991-2015, http://www.atmos-chem-phys.net/15/3991/2015/, 2015.

Dacre, H. F., Grant, A. L. M., and Johnson, B. T.: Aircraft observations and model simulations of concentration and particle size distribution in the Eyjafjallajökull volcanic ash cloud, Atmospheric Chemistry and Physics, 13, 1277–1291, doi:10.5194/acp-13-1277-2013, http://www.atmos-chem-phys.net/13/1277/2013/, 2013.

Dagan, G.: Lidar - Range-Resolved Optical Remote Sensing of the Atmosphere, Springer Verlag Gmbh, 2008.

Draine, B. T. and Flatau, P. J.: Discrete-Dipole Approximation For Scattering Calculations, J. Opt. Soc. Am. A, 11, 1491–1499, doi:10.1364/JOSAA.11.001491, http://josaa.osa.org/abstract.cfm?URI=josaa-11-4-1491, 1994.

Emeis, S., Schäfer, K., and Münkel, C.: Observation of the structure of the urban boundary layer with different ceilometers and validation by RASS data, Meteorologische Zeitschrift, 18, 149–154, doi:10.1127/0941-2948/2009/0365, 2009.

Emeis, S., Forkel, R., Junkermann, W., Schäfer, K., Flentje, H., Gilge, S., Fricke, W., Wiegner, M., Freudenthaler, V., Groß, S., Ries, L., Meinhardt, F., Birmili, W., Münkel, C., Obleitner, F., and Suppan, P.: Measurement and simulation of the 16/17 April 2010 Eyjafjallajökull volcanic ash layer dispersion in the northern Alpine region, Atmospheric Chemistry and Physics, 11, 2689–2701, doi:10.5194/acp-11-2689-2011, http://www.atmos-chem-phys.net/11/2689/2011/, 2011.

Flentje, H., Claude, H., Elste, T., Gilge, S., Köhler, U., Plass-Dülmer, C., Steinbrecht, W., Thomas, W., Werner, A., and Fricke, W.: The Eyjafjallajökull eruption in April 2010 – detection of volcanic plume using in-situ measurements, ozone sondes and lidar-ceilometer profiles, Atmospheric Chemistry and Physics, 10, 10 085–10 092, doi:10.5194/acp-10-10085-2010, http://www.atmos-chem-phys.net/10/10085/2010/, 2010a.

Flentje, H., Heese, B., Reichardt, J., and Thomas, W.: Aerosol profiling using the ceilometer network of the German Meteorological Service, Atmospheric Measurement Techniques Discussions, 3, 3643–3673, doi:10.5194/amtd-3-3643-2010, http://www.atmos-meas-tech-discuss.net/3/3643/2010/, 2010b.

Gasteiger, J., Groß, S., Freudenthaler, V., and Wiegner, M.: Volcanic ash from Iceland over Munich: mass concentration retrieved from ground-based remote sensing measurements, Atmospheric Chemistry and Physics, 11, 2209–2223, doi:10.5194/acp-11-2209-2011, http://www.atmos-chem-phys.net/11/2209/2011/, 2011a.

Gasteiger, J., Wiegner, M., Groß, S., Freudenthaler, V., Toledano, C., Tesche, M., and Kandler, K.: Modelling lidar-relevant optical properties of complex mineral dust aerosols, Tellus B, 63, http://www.tellusb.net/index.php/tellusb/article/view/16372, 2011b.

Groß, S., Freudenthaler, V., Wiegner, M., Gasteiger, J., Geiß, A., and Schnell, F.: Dual-wavelength linear depolarization ratio of volcanic aerosols: Lidar measurements of the Eyjafjallajökull plume over Maisach, Germany, Atmospheric Environment, 48, 85 – 96, doi:http://dx.doi.org/10.1016/j.atmosenv.2011.06.017, http://www.sciencedirect.com/science/article/pii/S1352231011006108, volcanic ash over Europe during the eruption of Eyjafjallajöekull on Iceland, April-May 2010, 2012.

Haarig, M., Engelmann, R., Ansmann, A., Veselovskii, I., Whiteman, D. N., and Althausen, D.: 1064 nm rotational Raman lidar for particle extinction and lidar-ratio profiling: cirrus case study, Atmospheric Measurement Techniques, 9, 4269–4278, doi:10.5194/amt-9-4269-2016, https://www.atmos-meas-tech.net/9/4269/2016/, 2016.

Hammann, E., Behrendt, A., Le Mounier, F., and Wulfmeyer, V.: Temperature profiling of the atmospheric boundary layer with rotational Raman lidar during the HD(CP)^2 Observational Prototype Experiment, Atmospheric Chemistry and Physics, 15, 2867–2881, doi:10.5194/acp-15-2867-2015, http://www.atmos-chem-phys.net/15/2867/2015/, 2015.

Kemppinen, O., Nousiainen, T., Merikallio, S., and Räisänen, P.: Retrieving microphysical properties of dust-like particles using ellipsoids: the case of refractive index, Atmospheric Chemistry and Physics, 15, 11 117–11 132, doi:10.5194/acp-15-11117-2015, http://www.atmos-chem-phys.net/15/11117/2015/, 2015.

Kokkalis, P., Papayannis, A., Amiridis, V., Mamouri, R. E., Veselovskii, I., Kolgotin, A., Tsaknakis, G., Kristiansen, N. I., Stohl, A., and Mona, L.: Optical, microphysical, mass and geometrical properties of aged volcanic particles observed over Athens, Greece, during the Eyjafjallajökull eruption in April 2010 through synergy of Raman lidar and sunphotometer measurements, Atmospheric Chemistry and Physics, 13, 9303–9320, doi:10.5194/acp-13-9303-2013, http://www.atmos-chem-phys.net/13/9303/2013/, 2013.

Lange, A. C. and Elbern, H.: Lidar data assimilation for improved analyses of volcanic aerosol events, in: Geophysical Research Abstracts, vol. 16 of *EGU2014-5987*, EGU General Assembly 2014, 2014.

Lathem, T. L., Kumar, P., Nenes, A., Dufek, J., Sokolik, I. N., Trail, M., and Russell, A.: Hygroscopic Properties of Volcanic Ash, geophysical Research letters, 2011.

Madonna, F., Amodeo, A., D'Amico, G., and Pappalardo, G.: A study on the use of radar and lidar for characterizing ultragiant aerosol, Journal of Geophysical Research: Atmospheres, 118, 10,056–10,071, doi:10.1002/jgrd.50789, http://dx.doi.org/10.1002/jgrd.50789, 2013.

Mallet, M., Tulet, P., Serça, D., Solmon, F., Dubovik, O., Pelon, J., Pont, V., and Thouron, O.: Impact of dust aerosols on the radiative budget, surface heat fluxes, heating rate profiles and convective activity over West Africa during March 2006, Atmospheric Chemistry and Physics, 9, 7143–7160, doi:10.5194/acp-9-7143-2009, http://www.atmos-chem-phys.net/9/7143/2009/, 2009.

Mamouri, R. E., Papayannis, A., Amiridis, V., Müller, D., Kokkalis, P., Rapsomanikis, S., Karageorgos, E. T., Tsaknakis, G., Nenes, A., Kazadzis, S., and Remoundaki, E.: Multi-wavelength Raman lidar, sun photometric and aircraft measurements in combination with inversion models for the estimation of the aerosol optical and physico-chemical properties over Athens, Greece, Atmospheric Measurement Techniques, 5, 1793–1808, doi:10.5194/amt-5-1793-2012, http://www.atmos-meas-tech.net/5/1793/2012/, 2012.

Matthias, V., Aulinger, A., Bieser, J., Cuesta, J., Geyer, B., Langmann, B., Serikov, I., Mattis, I., Minikin, A., Mona, L., Quante, M., Schumann, U., and Weinzierl, B.: The ash dispersion over Europe during the Eyjafjallajökull eruption – Comparison of CMAQ simulations to remote sensing and air-borne in-situ observations, Atmospheric Environment, 48, 184 – 194, doi:http://dx.doi.org/10.1016/j.atmosenv.2011.06.077, http://www.sciencedirect.com/science/article/pii/S1352231011007011, volcanic ash over Europe during the eruption of Eyjafjallajöekull on Iceland, April-May 2010, 2012.

Mie, G.: Beiträge zur Optik trüber Median, speziell kolloidaler Metallösungen, Annalen der Physik, doi:10.1002/andp.19083300302, 1908.

Mishchenko, M. I. and Travis, L. D.: Capabilities And Limitations Of A Current Fortran Implementation Of The 1-matrix Method For Randomly Oriented, Rotationally Symmetric Scatterers, Journal of Quantitative Spectroscopy and Radiative Transfer, 60, 309–324, 1998.

Mishchenko, M. I., Travis, L. D., and Lacis, A. A.: Scattering, Absorption, and Emission of Light by Small Particles, Cambridge University Press, 2002.

Mona, L., Amodeo, A., D'Amico, G., Giunta, A., Madonna, F., and Pappalardo, G.: Multi-wavelength Raman lidar observations of the Eyjafjallajökull volcanic cloud over Potenza, southern Italy, Atmospheric Chemistry and Physics, 12, 2229–2244, doi:10.5194/acp-12-2229-2012, http://www.atmos-chem-phys.net/12/2229/2012/, 2012.

Morcrette, J.-J., Boucher, O., Jones, L., Salmond, D., Bechtold, P., Beljaars, A., Benedetti, A., Bonet, A., Kaiser, J. W., Razinger, M., Schulz, M., Serrar, S., Simmons, A. J., Sofiev, M., Suttie, M., Tompkins, A. M., and Untch, A.: Aerosol analysis and forecast in the European Centre for Medium-Range Weather Forecasts Integrated Forecast System: Forward modeling, Journal of Geophysical Research: Atmospheres, 114, n/a–n/a, doi:10.1029/2008JD011235, http://dx.doi.org/10.1029/2008JD011235, d06206, 2009.

Mortier, A., Goloub, P., Podvin, T., Deroo, C., Chaikovsky, A., Ajtai, N., Blarel, L., Tanre, D., and Derimian, Y.: Detection and characterization of volcanic ash plumes over Lille during the Eyjafjallajökull eruption, Atmospheric Chemistry and Physics, 13, 3705–3720, doi:10.5194/acp-13-3705-2013, http://www.atmos-chem-phys.net/13/3705/2013/, 2013.

Pappalardo, G., Amodeo, A., Apituley, A., Comeron, A., Freudenthaler, V., Linné, H., Ansmann, A., Bösenberg, J., D'Amico, G., Mattis, I., Mona, L., Wandinger, U., Amiridis, V., Alados-Arboledas, L., Nicolae, D., and Wiegner, M.: EARLINET: towards an advanced sustainable European aerosol lidar network, Atmospheric Measurement Techniques, 7, 2389–2409, doi:10.5194/amt-7-2389-2014, http://www.atmos-meas-tech.net/7/2389/2014/, 2014.

Radlach, M., Behrendt, A., and Wulfmeyer, V.: Scanning rotational Raman lidar at 355 nm for the measurement of tropospheric temperature fields, Atmospheric Chemistry and Physics, 8, 159–169, doi:10.5194/acp-8-159-2008, http://www.atmos-chem-phys.net/8/159/2008/, 2008.

Rieger, D., Bangert, M., Kottmeier, C., Vogel, H., and Vogel, B.: Impact of aerosol on post-frontal convective clouds over Germany, Tellus B, 66, http://www.tellusb.net/index.php/tellusb/article/view/22528, 2014.

Rocha-Lima, A., Martins, J. V., Remer, L. A., Krotkov, N. A., Tabacniks, M. H., Ben-Ami, Y., and Artaxo, P.: Optical, microphysical and compositional properties of the Eyjafjallajökull volcanic ash, Atmospheric Chemistry and Physics, 14, 10 649–10 661, doi:10.5194/acp-14-10649-2014, http://www.atmos-chem-phys.net/14/10649/2014/, 2014.

Sandrini, S., Giulianelli, L., Decesari, S., Fuzzi, S., Cristofanelli, P., Marinoni, A., Bonasoni, P., Chiari, M., Calzolai, G., Canepari, S., Perrino, C., and Facchini, M. C.: In situ physical and chemical characterisation of the Eyjafjallajökull aerosol plume in the free troposphere over Italy, Atmospheric Chemistry and Physics, 14, 1075–1092, doi:10.5194/acp-14-1075-2014, http://www.atmos-chem-phys.net/14/1075/2014/, 2014.

Schumann, U., Weinzierl, B., Reitebuch, O., Schlager, H., Minikin, A., Forster, C., Baumann, R., Sailer, T., Graf, K., Mannstein, H., Voigt, C., Rahm, S., Simmet, R., Scheibe, M., Lichtenstern, M., Stock, P., Rüba, H., Schäuble, D., Tafferner, A., Rautenhaus, M., Gerz, T., Ziereis, H., Krautstrunk, M., Mallaun, C., Gayet, J.-F., Lieke, K., Kandler, K., Ebert, M., Weinbruch, S., Stohl, A., Gasteiger, J., Groß, S., Freudenthaler, V., Wiegner, M., Ansmann, A., Tesche, M., Olafsson, H., and Sturm, K.: Airborne observations of the Eyjafjalla volcano ash cloud over Europe during air space closure in April and May 2010, Atmospheric Chemistry and Physics, 11, 2245–2279, doi:10.5194/acp-11-2245-2011, http://www.atmos-chem-phys.net/11/2245/2011/, 2011.

Shipley, S. T., Tracy, D. H., Eloranta, E. W., Trauger, J. T., Sroga, J. T., Roesler, F. L., and Weinman, J. A.: High spectral resolution lidar to measure optical scattering properties of atmospheric aerosols. 1: Theory and instrumentation, Appl. Opt., 22, 3716–3724, doi:10.1364/AO.22.003716, http://ao.osa.org/abstract.cfm?URI=ao-22-23-3716, 1983.

SIČ, B.: Amélioration de la représentation des aérosols dans un modèle de chimie-transport : Modélisation et assimilation de donnèes, Ph.D. thesis, Université Toulouse, 2014.

Späth, F., Behrendt, A., Muppa, S. K., Metzendorf, S., Riede, A., and Wulfmeyer, V.: 3D Water Vapor Field in the Atmospheric Boundary Layer Observed with Scanning Differential Absorption Lidar, Atmospheric Measurement Techniques Discussions, 2016, 1–40, doi:10.5194/amt-2015-393, http://www.atmos-meas-tech-discuss.net/amt-2015-393/, 2016.

Strohbach, J.: Ausbreitung der Eyjafjallajökull-Vulkanasche im April 2010 über Deutschland: Reanalyse der Ceilometermessungen des Deutschen Wetterdienstes, bachelor Thesis, 2015.

Sugimoto, N., Matsui, I., Shimizu, A., Nishizawa, T., Hara, Y., Xie, C., Uno, I., Yumimoto, K., Wang, Z., and Yoon, S.-C.: Lidar network observations of tropospheric aerosols, in: Lidar Remote Sensing for Environmental Monitoring IX, vol. 7153, pp. 71 530A–71 530A–13, doi:10.1117/12.806540, http://dx.doi.org/10.1117/12.806540, 2008.

Turner, D. D., Ferrare, R. A., Heilman Brasseur, L. A., Feltz, W. F., and Tooman, T. P.: Automated Retrievals of Water Vapor and Aerosol Profiles from an Operational Raman Lidar, Journal of Atmospheric and Oceanic Technology, 19, 2002.

Vogel, B., Vogel, H., Bäumer, D., Bangert, M., Lundgren, K., Rinke, R., and Stanelle, T.: The comprehensive model system COSMO-ART – Radiative impact of aerosol on the state of the atmosphere on the regional scale, Atmospheric Chemistry and Physics, 9, 8661–8680, doi:10.5194/acp-9-8661-2009, http://www.atmos-chem-phys.net/9/8661/2009/, 2009.

Vogel, H., Förstner, J., Vogel, B., Hanisch, T., Mühr, B., Schättler, U., and Schad, T.: Time-lagged ensemble simulations of the dispersion of the Eyjafjallajökull plume over Europe with COSMO-ART, Atmospheric Chemistry and Physics, 14, 7837–7845, doi:10.5194/acp-14-7837-2014, http://www.atmos-chem-phys.net/14/7837/2014/, 2014.

Waquet, F., Peers, F., Goloub, P., Ducos, F., Thieuleux, F., Derimian, Y., Riedi, J., Chami, M., and Tanré, D.: Retrieval of the Eyjafjallajökull volcanic aerosol optical and microphysical properties from POLDER/PARASOL measurements, Atmospheric Chemistry and Physics, 14, 1755–1768, doi:10.5194/acp-14-1755-2014, http://www.atmos-chem-phys.net/14/1755/2014/, 2014.

Whiteman, D. N., Melfi, S. H., and Ferrare, R. A.: Raman lidar system for the measurement of water vapor and aerosols in the Earth's atmosphere, Appl. Opt., 31, 3068–3082, doi:10.1364/AO.31.003068, http://ao.osa.org/abstract.cfm?URI=ao-31-16-3068, 1992.

Wiegner, M., Madonna, F., Binietoglou, I., Forkel, R., Gasteiger, J., Geiß, A., Pappalardo, G., Schäfer, K., and Thomas, W.: What is the benefit of ceilometers for aerosol remote sensing? An answer from EARLINET, Atmospheric Measurement Techniques, 7, 1979–1997, doi:10.5194/amt-7-1979-2014, http://www.atmos-meas-tech.net/7/1979/2014/, 2014.

Wiscombe, W. J.: Improved Mie scattering algorithms, Optical Society of America, 19, 1980.

Wolke, R., Hellmuth, O., Knoth, O., Schröder, W., Heinrich, B., and Renner, E.: Air Pollution Modeling and Its Application XVI, chap. The Chemistry-Transport Modeling System lm-Muscat: Description and citydelta Applications, pp. 427–439, Springer US, Boston, MA, doi:10.1007/978-1-4419-8867-6_39, http://dx.doi.org/10.1007/978-1-4419-8867-6_39, 2004.

Wulfmeyer, V. and Feingold, G.: On the relationship between relative humidity and particle backscattering coefficient in the marine boundary layer determined with differential absorption lidar, Journal of Geophysical Research: Atmospheres, 105, 4729–4741, doi:10.1029/1999JD901030, http://dx.doi.org/10.1029/1999JD901030, 2000.

Wulfmeyer, V., Pal, S., Turner, D. D., and Wagner, E.: Can Water Vapour Raman Lidar Resolve Profiles of Turbulent Variables in the Convective Boundary Layer?, Boundary-Layer Meteorology, 136, 253–284, doi:10.1007/s10546-010-9494-z, http://dx.doi.org/10.1007/s10546-010-9494-z, 2010.

Wulfmeyer, V., Hardesty, R. M., Turner, D. D., Behrendt, A., Cadeddu, M. P., Di Girolamo, P., Schlüssel, P., Van Baelen, J., and Zus, F.: A review of the remote sensing of lower tropospheric thermodynamic profiles and its indispensable role for the understanding and the simulation of water and energy cycles, Reviews of Geophysics, 53, 819–895, doi:10.1002/2014RG000476, http://dx.doi.org/10.1002/2014RG000476, 2014RG000476, 2015.

Young, A. T.: Rayleigh scattering, Optical Society of America, 20, 533–535, 1981.

Zakey, A. S., Solmon, F., and Giorgi, F.: Implementation and testing of a desert dust module in a regional climate model, Atmospheric Chemistry and Physics, 6, 4687–4704, doi:10.5194/acp-6-4687-2006, http://www.atmos-chem-phys.net/6/4687/2006/, 2006.

Zakšek, K., Hort, M., Zaletelj, J., and Langmann, B.: Monitoring volcanic ash cloud top height through simultaneous retrieval of optical data from polar orbiting and geostationary satellites, Atmospheric Chemistry and Physics, 13, 2589–2606, doi:10.5194/acp-13-2589-2013, http://www.atmos-chem-phys.net/13/2589/2013/, 2013.

Table 1. Output variables of COSMO-ART used by the forward operator for the selected case study.

Variable	Symbol	Description	Unit
$ASH1$	N_1	Ash number density of class 1 (1 µm)	m^{-3}
$ASH2$	N_2	Ash number density of class 2 (3 µm)	m^{-3}
$ASH3$	N_3	Ash number density of class 3 (5 µm)	m^{-3}
$ASH4$	N_4	Ash number density of class 4 (10 µm)	m^{-3}
$ASH5$	N_5	Ash number density of class 5 (15 µm)	m^{-3}
$ASH6$	N_6	Ash number density of class 6 (30 µm)	m^{-3}
$Pmain$	p	Atmospheric pressure	hPa
T	T	Atmospheric temperature	°C

Table 2. Settings of the T-matrix procedure for the particle shape sensitivity study. The parameters were kept constant during the study except the particle shape parameters (EPS and NP)

Variable	Value	Description
RAT	1	Radius is given as equal-sphere-volume radius
$NPNAX$	1	Setting for monodisperse distributions
$AXMAX$	1	Setting for monodisperse distributions
B	1D-1	Setting for monodisperse distribution
$NKMAX$	-1	Setting for monodisperse distributions
$NDISTR$	4	Setting for monodisperse distributions
EPS	0.5 ... 2.0	Aspect ratio of the scatterer
NP	-1 or -2	Selects the particle type (spheres NP=-1 or cylinders NP=-2)
LAM	1064.e-9	Wavelength of incoming light
MRR	1.59	Real part of the refractive index
MRI	-0.004	Imaginary part of the refractive index
$NPNA$	19	Number of random angles

Table 3. Effective optical cross sections ~~and average lidar ratio~~ of atmospheric gas molecules and six volcanic ash size ~~classes with their respective aerodynamic diameter~~calculated for the ACL wavelength ($\lambda = 1064\,\mathrm{nm}$). ~~The~~ While the effective ~~optical~~ extinction cross ~~sections were used by~~ section increases nearby exponentially with the ~~forward operator in~~ particle classes size, the ~~Eyjafjallajökull case study~~effective backscatter cross section does not even scale linearly with the particle size. In consequence, the ACL measured attenuated backscatter coefficient is less sensitive to number density variations of size class 6 than of size class 3 etc.

Scatterer Class	~~σ_{ext}~~ $\overline{\sigma_{\mathrm{ext}}}$ (m^2)	~~σ_{bsc}~~ $\overline{\sigma_{\mathrm{bsc}}}$ ($\mathrm{m}^2\,\mathrm{sr}^{-1}$) ~~$S_{\mathrm{lidar}}$ (sr)~~
Atmospheric Gas	3.125×10^{-32}	3.680×10^{-33} ~~8.49~~
Ash 1 (1 µm)	4.324×10^{-12}	0.328×10^{-12} ~~58.83~~
Ash 2 (3 µm)	17.821×10^{-12}	3.843×10^{-12} ~~5.23~~
Ash 3 (5 µm)	61.672×10^{-12}	6.200×10^{-12} ~~11.90~~
Ash 4 (10 µm)	177.045×10^{-12}	5.365×10^{-12} ~~64.16~~
Ash 5 (15 µm)	526.967×10^{-12}	20.442×10^{-12} ~~47.21~~
Ash 6 (30 µm)	1937.387×10^{-12}	23.781×10^{-12} ~~179.58~~

Table 4. Point-data extraction of COMSO-ART output at ACL station Deuselbach; ~~case~~ coordinate 1 ~~from~~ is at 16 April 2010, 18:00 UTC, in a height of 1.9 km ASL. Using the number density N_d of volcanic ash class d, ~~we calculated~~ the individual backscatter coefficient $\beta_{\mathrm{par},d,\lambda}$, the contribution to the total backscatter coefficient $\sum \beta_{\mathrm{par},d,\lambda}$, the individual mass density ρ_d, and the contribution to the total mass density $\sum \rho_d$ were calculated. Ash particles were ~~treated as spherical objects with~~ calculated using a volumetric mass density of $2500\,\mathrm{kg\,m^{-3}}$. A non-linear relationship between the relative contribution to the total backscatter coefficient and the relative contribution to the transported mass of an ash size class can be observed: While the first three classes contribute by 95 % to the total backscatter coefficient, they carry only 78 % of the volcanic ash mass. This dependency to the laser wavelength can be used as advantage for multi-wavelength lidar systems.

d	N_d	$\beta_{\mathrm{par},d,\lambda}$	$\frac{\beta_{\mathrm{par},d,\lambda}}{\sum \beta_{\mathrm{par},d,\lambda}}$	ρ_d	$\frac{\rho_d}{\sum \rho_d}$
-	$\mathrm{m^{-3}}$	$\mathrm{m^{-1}\,sr^{-1}}$	-	$\mathrm{kg\,m^{-3}}$	-
1	43 653 522	1.4×10^{-5}	22.3 %	0.57×10^{-7}	3.3 %
2	7 044 794	2.7×10^{-5}	41.9 %	2.49×10^{-7}	14.2 %
3	3 194 338	2.0×10^{-6}	30.7 %	5.23×10^{-7}	29.8 %
4	462 402	2.5×10^{-6}	3.8 %	6.05×10^{-7}	34.5 %
5	37 161	7.6×10^{-7}	1.2 %	1.64×10^{-7}	9.3 %
6	4474	1.1×10^{-7}	0.2 %	1.58×10^{-7}	9.0 %

Table 5. The same as Table 4 but for ~~case~~ coordinate 2 at 16 April 2010, 09:00 UTC, in a height of 1.5 km ASL. Even if class 4 carries only 27 % of the mass, it contributes by 67 % to the total backscatter coefficient. The inverse situation can be observed for the size class 6 which holds 73 % of the mass but contributes only by 30 % to the backscatter coefficient at this coordinate.

d	N_d	$\beta_{\mathrm{par},d,\lambda}$	$\frac{\beta_{\mathrm{par},d,\lambda}}{\sum \beta_{\mathrm{par},d,\lambda}}$	ρ_d	$\frac{\rho_d}{\sum \rho_d}$
-	m^{-3}	$\mathrm{m}^{-1}\,\mathrm{sr}^{-1}$	-	$\mathrm{kg\,m}^{-3}$	-
1	93.0	30.7×10^{-12}	0.2 %	0.01×10^{-9}	0.1 %
2	97.0	372.5×10^{-12}	2.8 %	0.01×10^{-9}	0.1 %
3	1.0	6.2×10^{-12}	0.1 %	0.01×10^{-9}	0.1 %
4	1700.0	9129.0×10^{-12}	67.3 %	2.23×10^{-9}	27.1 %
5	0.5	10.2×10^{-12}	0.1 %	0.01×10^{-9}	0.1 %
6	169.0	4018.8×10^{-12}	29.6 %	5.97×10^{-9}	72.8 %

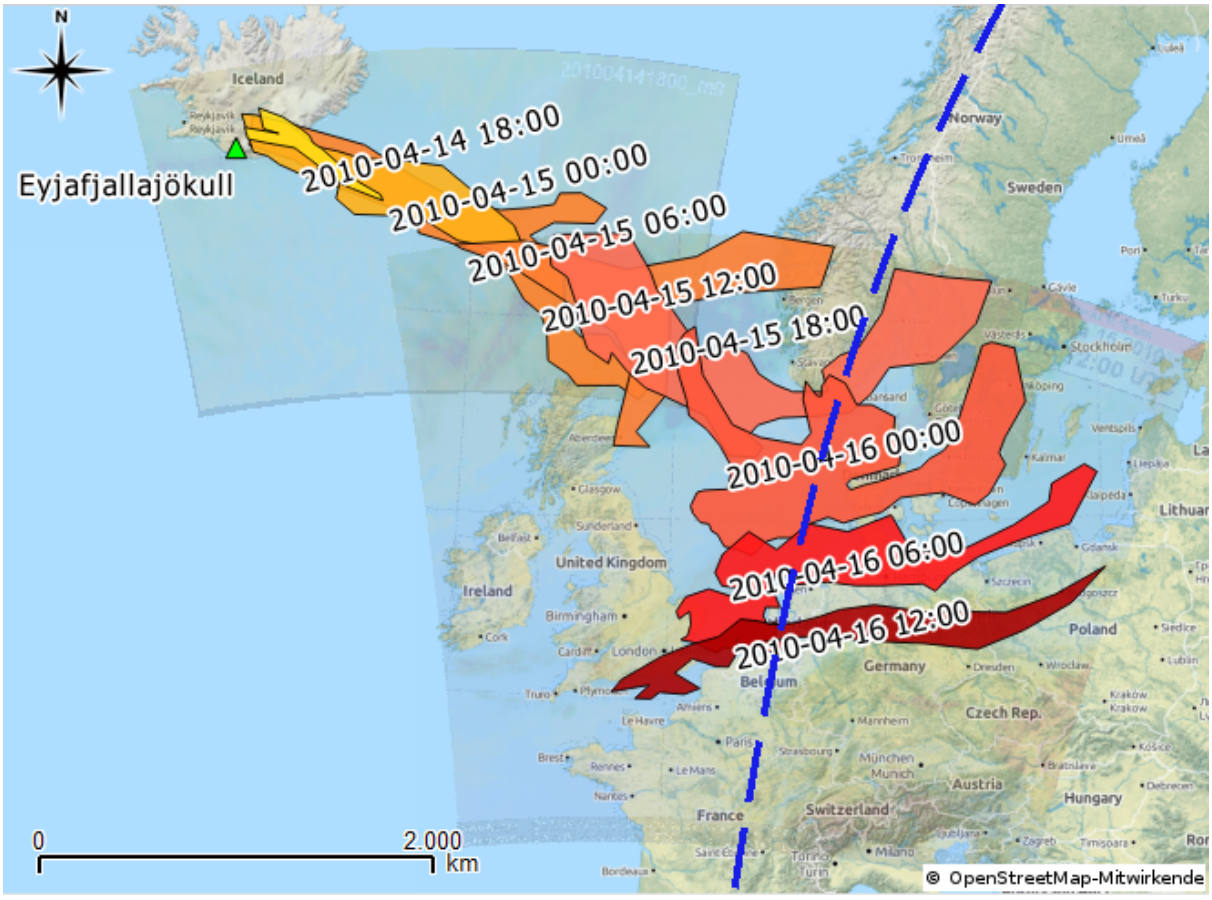

Figure 1. Distribution and transport of volcanic ash over northwest Europe sketched using georeferenced satellite images (Meteosat-9, Dust). After georeferencing, the ash layers were retraced as colored polygons, where the color of the polygons (yellow to red) represent consecutive time steps (Strohbach, 2015). The blue dashed line indicates the flight track of CALIPSO during 17 April 2010 (~~6 hour time steps~~)measurement shown in Fig. 2)

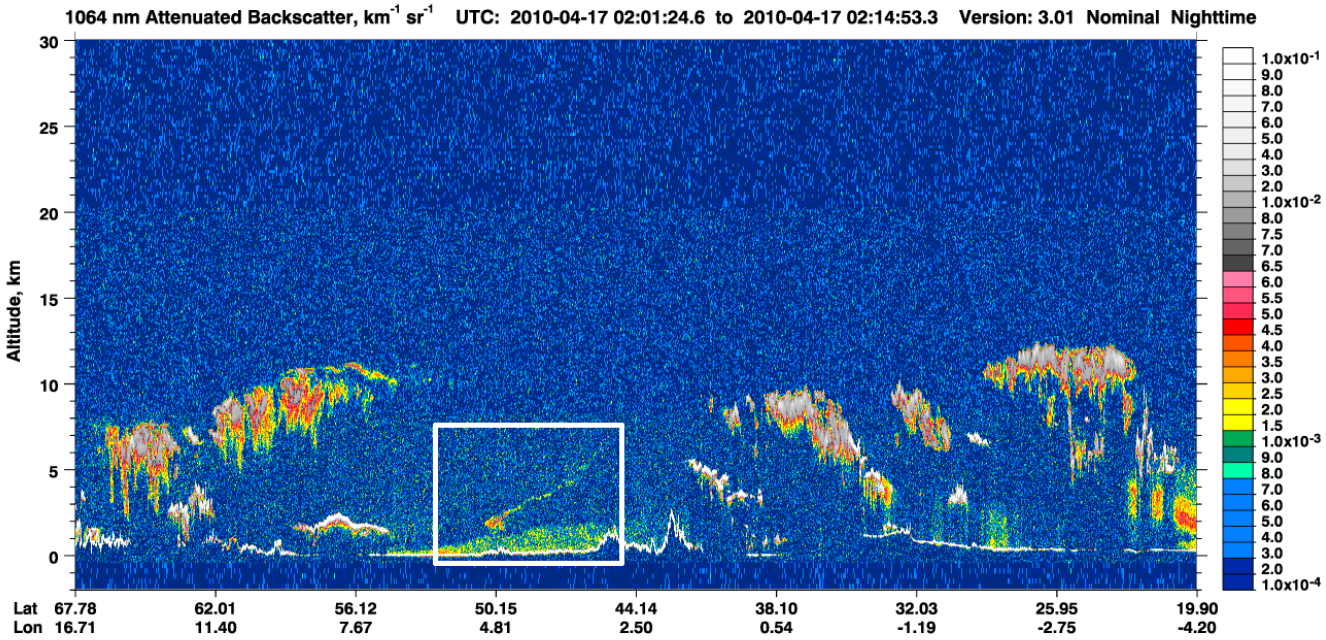

Figure 2. Attenuated backscatter coefficient measurement from CALIOP ~~which was~~ used to calibrate the ACL measurement during the Eyjafjallajökull eruption phase. The volcanic ash ~~cloud~~ plume is visible around 50.15° lat and 4.81° lon. As the instrument measures from space, the values of the attenuated backscatter coefficient inside the ash plume is not affected by attenuation due to aerosols in the planetary boundary layer. Image obtained from http://www-calipso.larc.nasa.gov/

~~The German ACL network in 2010. Each dot represents an ACL station and the dot color is an indicator for the ash layer visibility within the measurement. Red color: Near-ground fog or water clouds cover the ash cloud, orange: ash clouds are almost (yellow: partially) covered by fog or clouds, green: clean air situation with a full view on the ash layers.~~

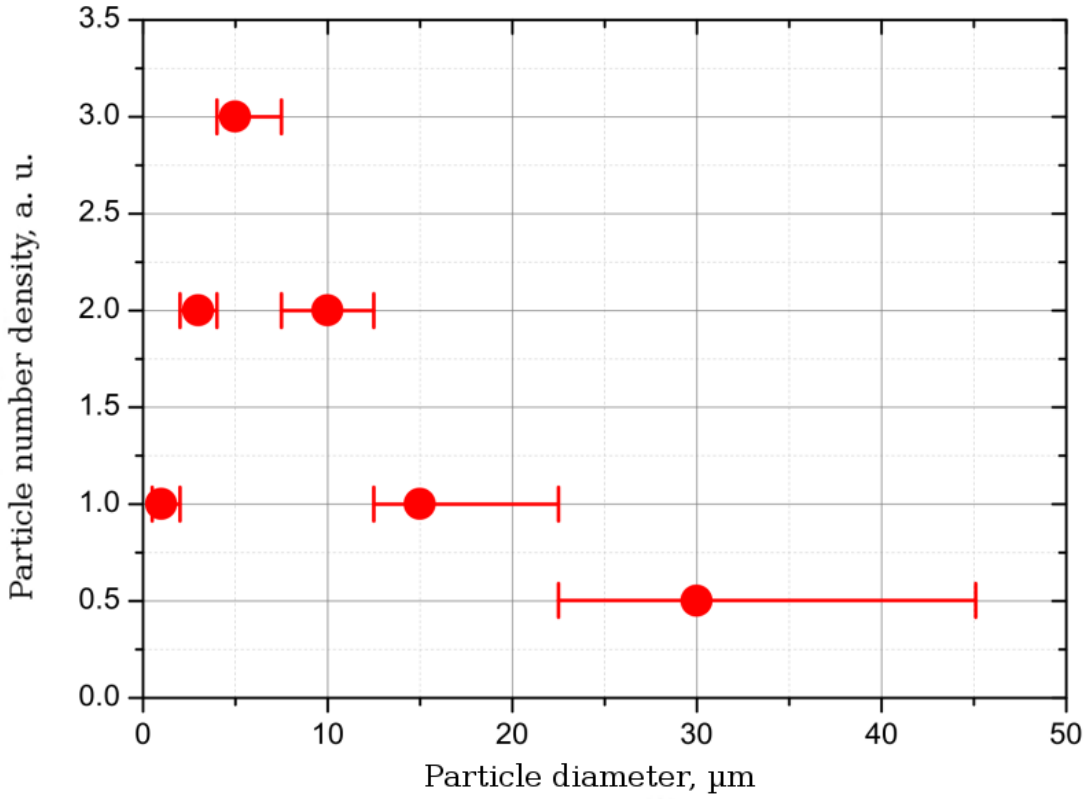

Figure 3. Sketch of the particle size distribution represented by COSMO-ART ~~within~~ for the ~~case study~~ Eyjafjallajökull dispersion simulation (red dots). The red lines with bars indicate the averaging margins ~~we~~ that were defined for the calculation of effective optical cross sections.

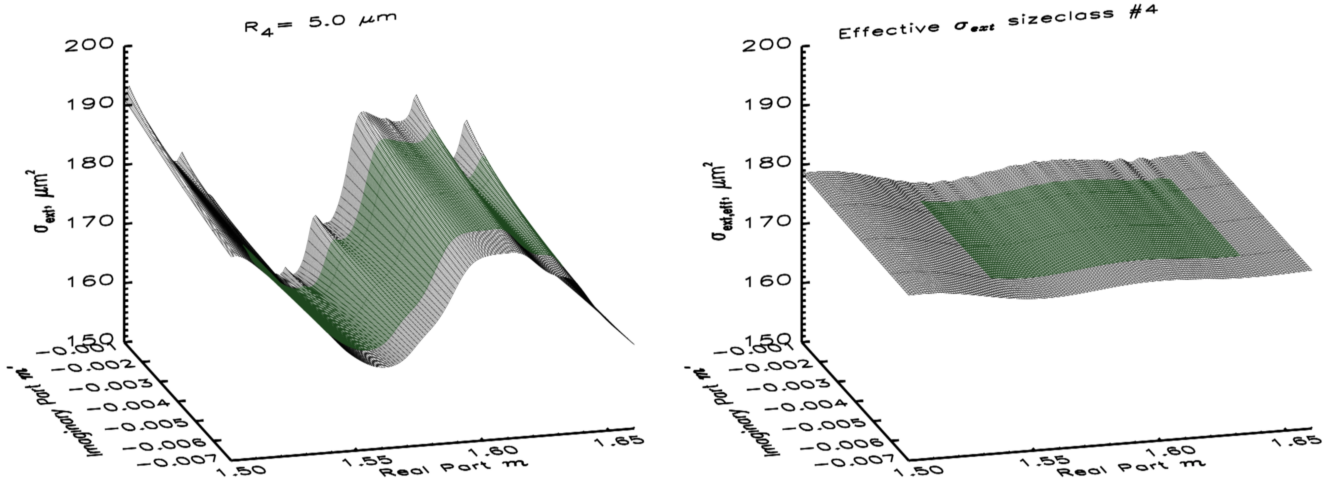

Figure 4. Sensitivity of σ_{ext} to the real and imaginary part of the refractive index for a single particle radius R_p (left) and after calculating the effective extinction cross section $\overline{\sigma_{\mathrm{ext}}}$ (right). The green shaded area is the ~~relevant~~ considered range of real part m and imaginary part m' for the uncertainty estimation as explained in section 4.1.

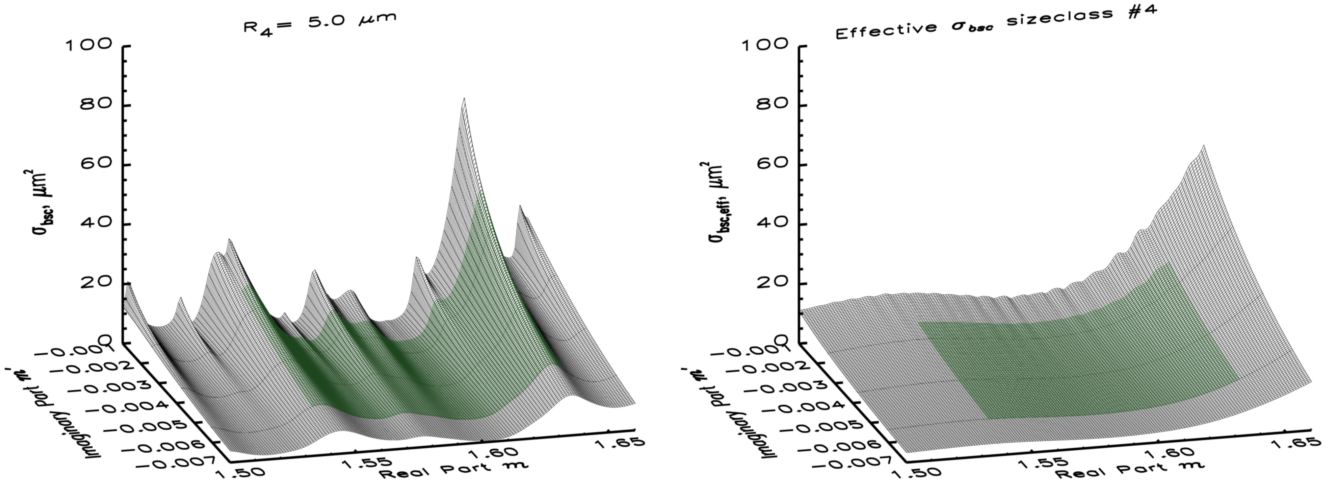

Figure 5. The same as Fig. 4 but for the backscatter cross section $\sigma_{\rm bsc}$ (left) and the effective backscatter cross section $\overline{\sigma_{\rm bsc}}$ (right). The backscatter cross section is very sensitive to the refractive index. While the major fraction of backscatter cross section variations can be removed by calculating the effective backscatter cross section, the sensitivity at the extreme end of the defined refractive index remains.

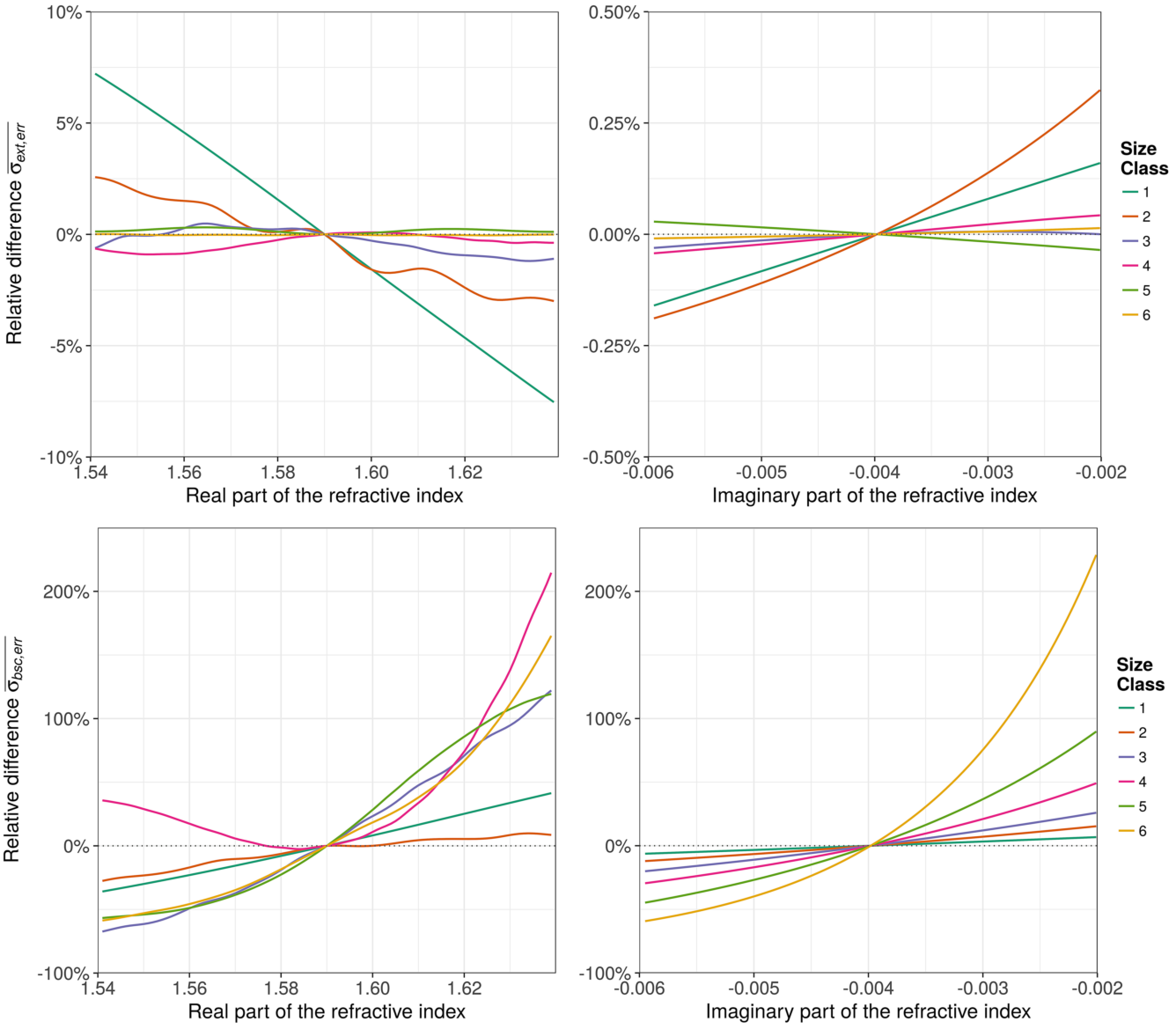

Figure 6. Relative errors of the effective extinction cross section (top row) and of the effective backscatter cross section (bottom row) if the assumed reference refractive index (~~red dot~~1.59 - 0.004i) ~~is not equal~~ varies to the true refractive index. ~~Plots in the left row show the error for variable imaginary parts; plots in the right row for variable~~ Uncertain real parts of the refractive index ~~. Uncertainties of the imaginary part~~ (left column) may lead to ~~a maximum error~~ errors of ~~0.5~~7% for the effective extinction cross section ~~and~~ as well as of ~~230~~225% for the effective backscatter cross section. Uncertain ~~real~~ imaginary parts ~~also~~ of the refractive index (right column) may lead to ~~errors~~ a maximum error of ~~7~~0.5% for the effective extinction cross section ~~as well as~~ and of ~~225~~230% for the effective backscatter cross section~~in~~. The maximum error was observed at the ~~worst case~~outer range of considered refractive indices. So reducing the considered range of refractive indices reduces the maximum error of the effective extinction and backscatter cross section.

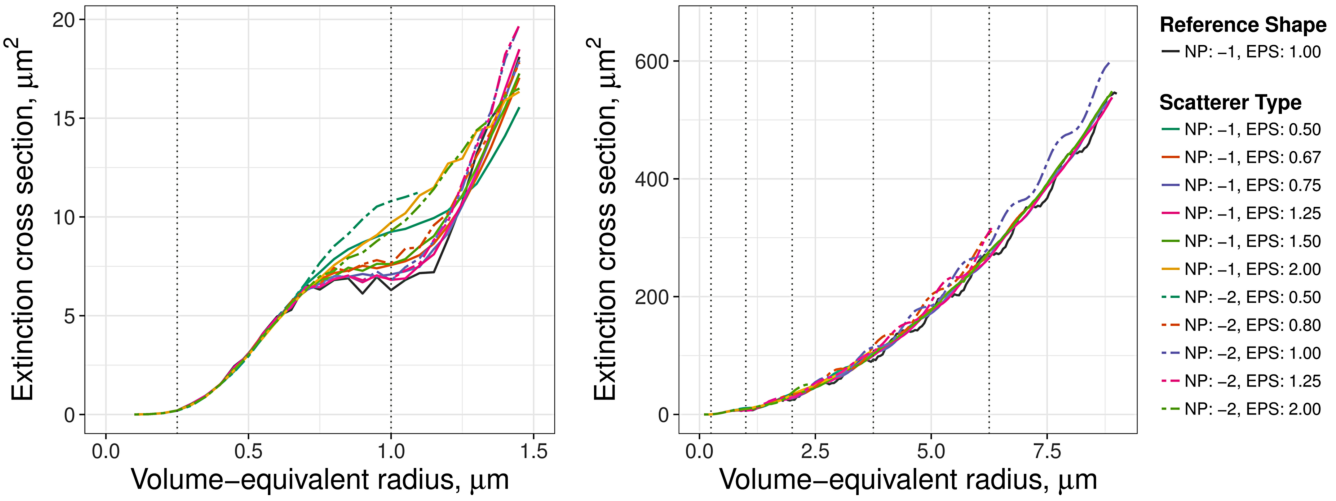

Figure 7. Extinction cross section spectrum for the reference particle (sphere, dark grey line), six types of ellipsoids (EPS=1, solid lines), and 5 types of cylinders (EPS=-2, dashed lines) against the particles' equal-volume radius R_p at $\lambda = 1064\,\mathrm{nm}$. ~~The~~ Vertical dotted lines indicate the size-margins of each class. The particle shape effect is negligible for particles with a radius much smaller than the wavelength. Particles which have a radius equal to the wavelength show differences of the extinction cross section depending on their shape. With larger particle sizes, the particle shape effect is negligible for the considered shapes and aspect ratios.

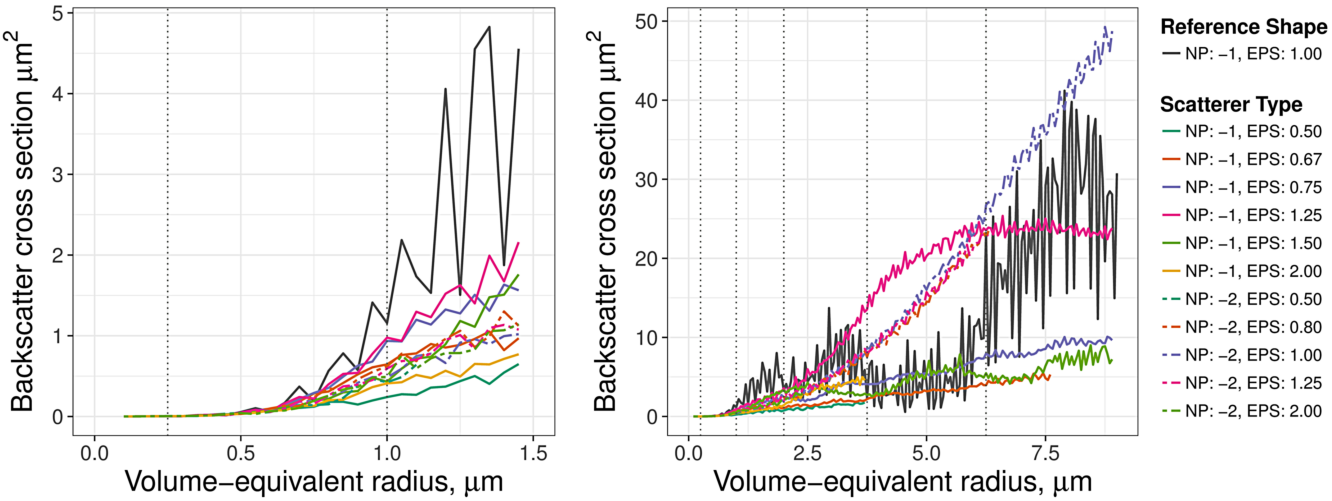

Figure 8. The same as Fig. 7 but for the backscatter cross section. A high particle shape sensitivity of the backscatter cross section can be observed which becomes pronounced for particles with radius greater than 0.5λ. While the backscatter cross section of ellipsoids increases only weakly with particle size, the backscatter cross section of cylinders increases nearby exponentially with size. The backscatter cross section spectrum of spheres has larger-scale fluctuations which are due to interference effects. For particle size classes 4 and 5, the backscatter cross section of spheres is between the values of ellipsoids and cylinders which indicates that a spherical shape is a valid representative for large volcanic ash size classes

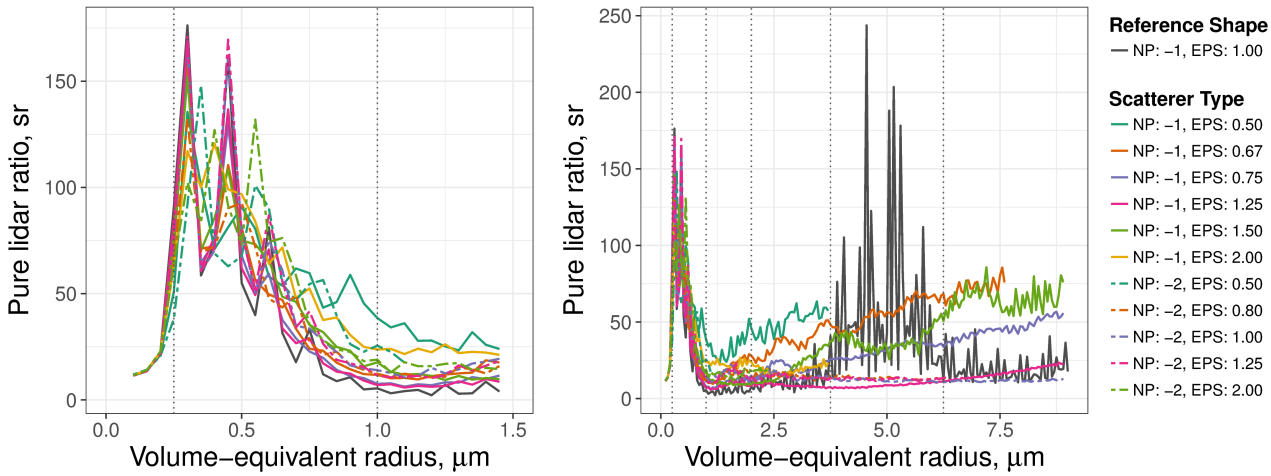

Figure 9. The same as Fig. 7 but for the pure lidar ratio. Similar to the observations for the backscatter cross section (see Fig. 8), the particle shape sensitivity of the pure lidar ratio is negligible for particles smaller than 0.5λ. For larger particles, the spherical shape tends to have the lowest pure lidar ratio value of all particle shapes (namely for a particle radius between 0.5 µm and 3.5 µm. Peaks of the pure lidar ratio are observed for spheres with a radius between 4 µm and 6 µm which are due to interference effects. Large ellipsoids tend to have the highest pure lidar ratio values in comparison with other particle shapes; large cylinders have an almost constant value of the pure lidar ratio of about 15 sr.

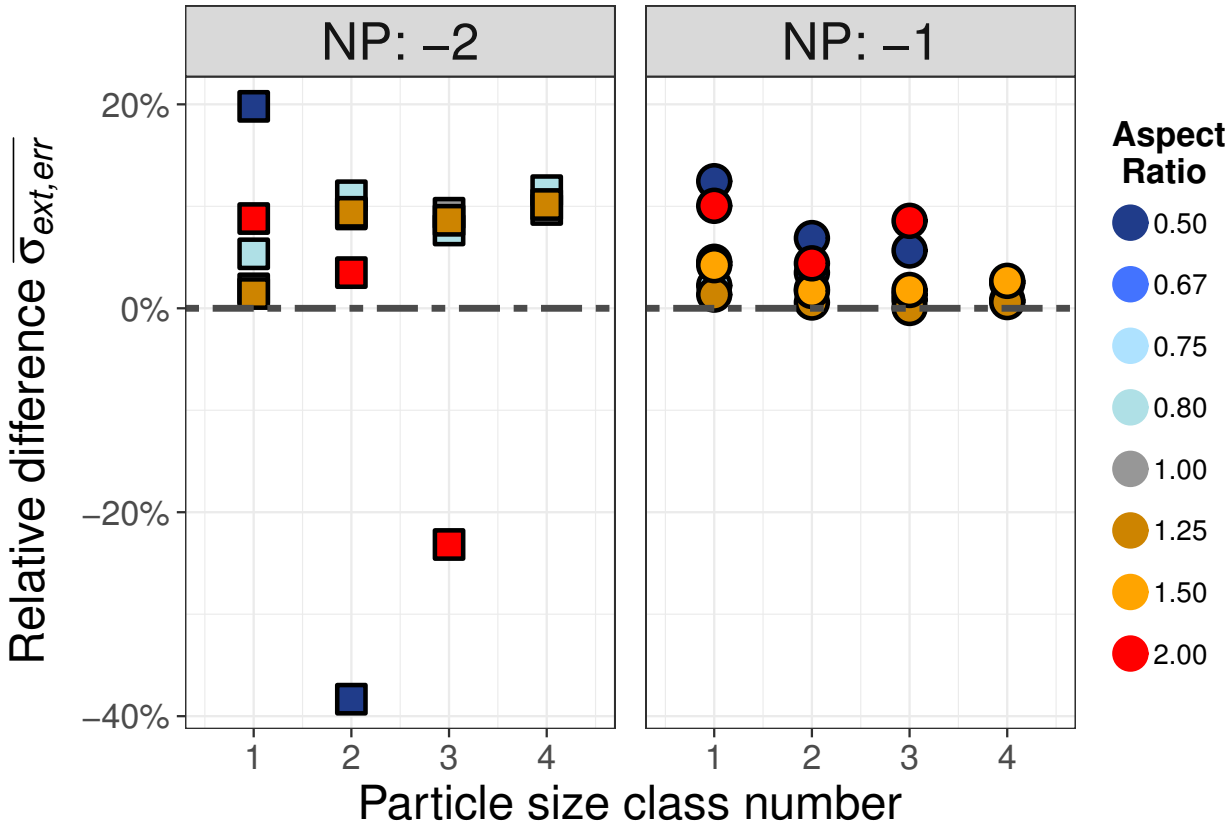

Figure 10. Relative errors of the effective extinction cross section if spherical particles are assumed but the real particles ~~would be of~~ have an elliptical (NP: -1) or cylindrical shape (NP: -2). Negative ~~(positive)~~ values indicate that spherical particles have a larger ~~(smaller)~~ effective extinction cross section ~~. Except for a strongly asymmetric cylinder, the effective extinction cross section of spherical~~ than equal-sized non-spherical particles and vice versa. The maximum relative differences are ~~mostly smaller (up to 12 %)~~11 % and −35 %.

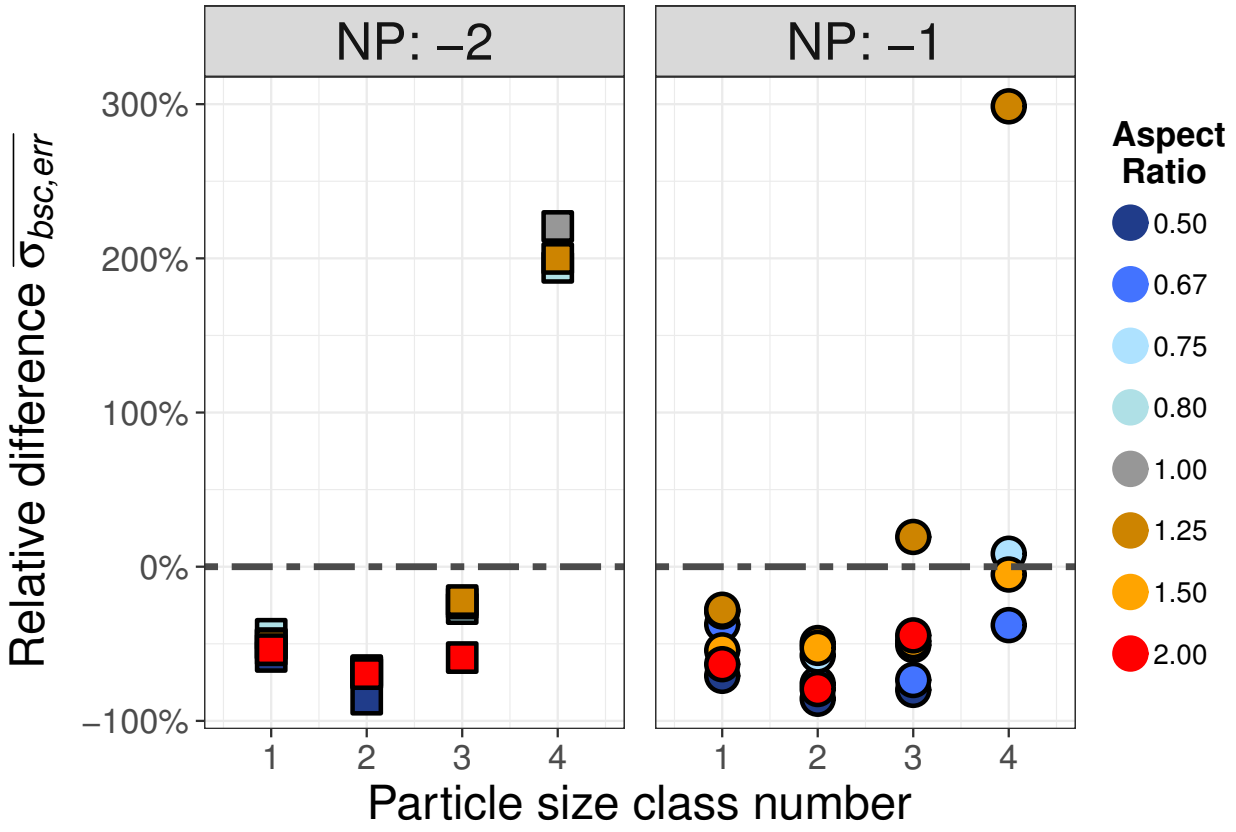

Figure 11. The same as Fig. 10 but for the effective backscatter cross section. The maximum relative difference between the effective backscatter cross section of spherical and non-spherical particles are observed for size class 2 with a relative difference of up to −80 % (resulting in a difference factor of 5). But also for other size classes, the relative difference is about factor 2 when assuming spherical shape for the considered non-spherical particle shapes.

~~The same as Fig. 10 and 11 but for the effective lidar ratio.~~

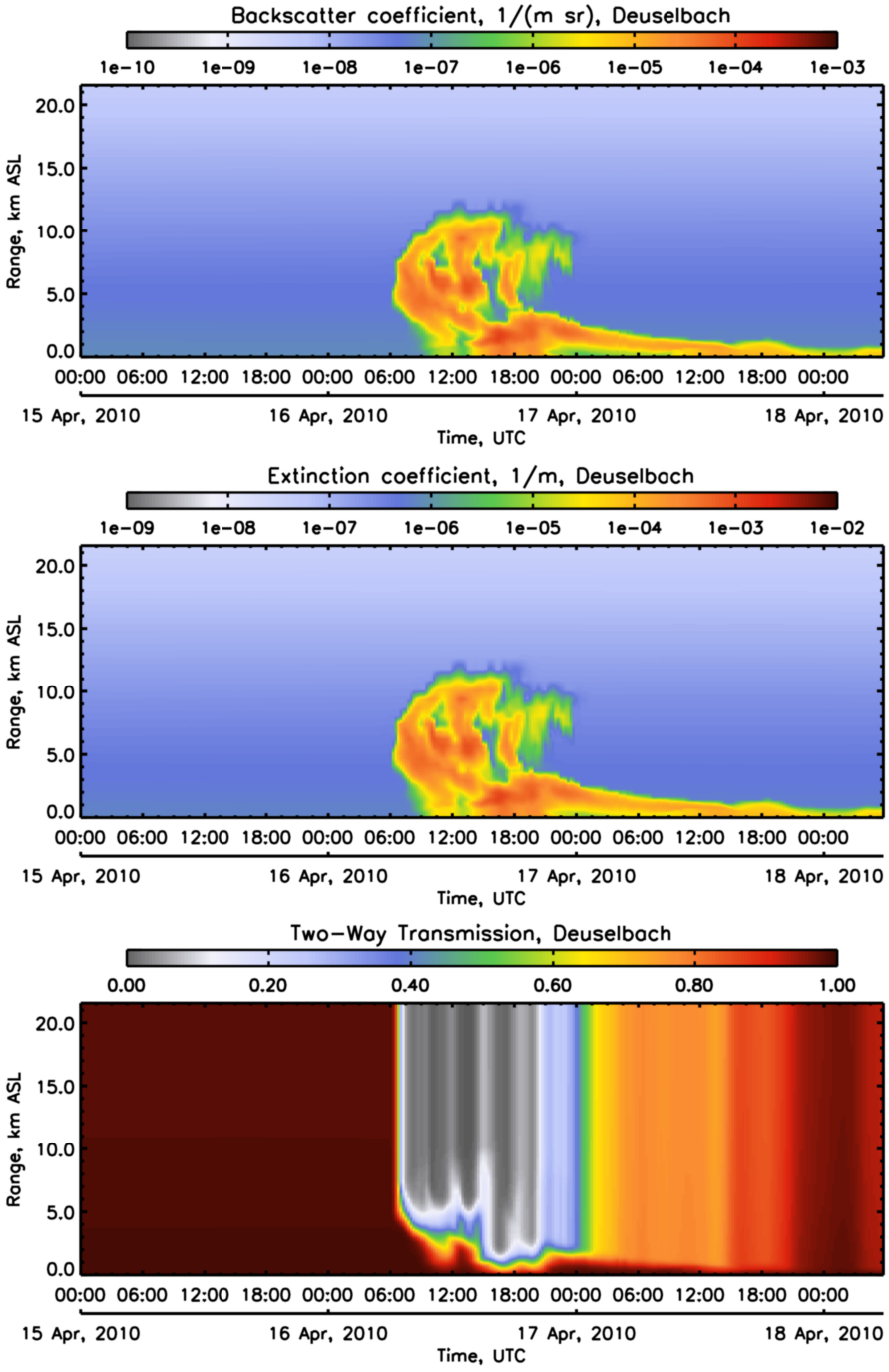

Figure 12. Time-height cross section of total ~~extinction~~ backscatter coefficient, ~~backscatter~~ extinction coefficient, and two-way transmission, calculated by the forward model based on COSMO-ART output at the station Deuselbach (West Germany). The vertical coordinates are given in km above sea level (ASL). The forward model ~~represents clean air molecules~~ used temperature, pressure, and volcanic ash ~~particles~~ particle data (no clouds, rain, fog, background aerosol or other scattering objects). The backscatter coefficient is by about one order of magnitude lower than the extinction coefficient. The two-way transmission is nearby 1 over clean-air situations. Above ash layers, however, the two-way transmission has a value of only 5 %.

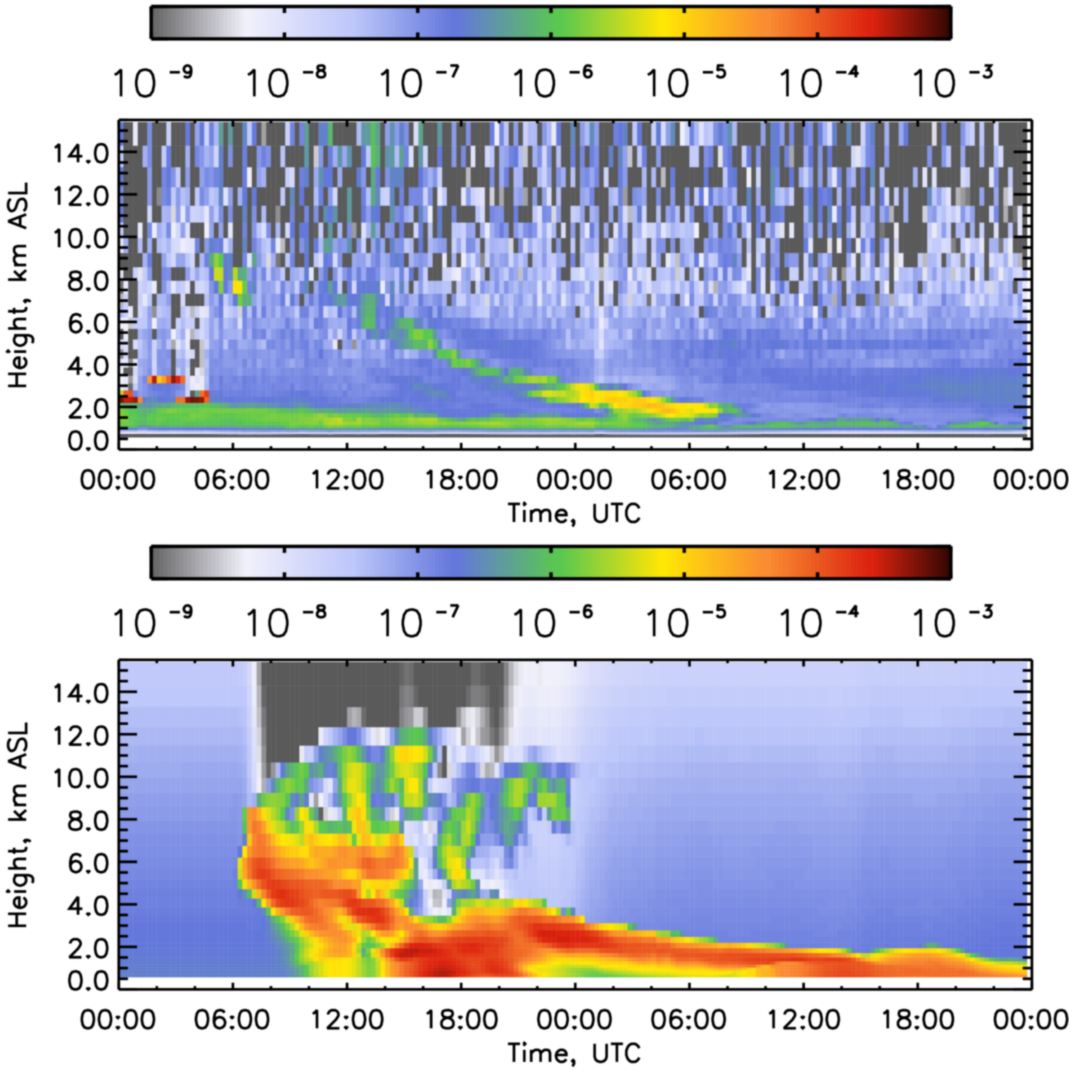

Figure 13. Attenuated backscatter coefficient of ceilometer (top) and forward model (bottom) at the station Deuselbach in Germany from ~~the 16th of~~ 16 April 2010, 00:00 UTC to ~~the 17th of~~ 17 April 2010, 24:00 UTC. The ACL measurements in heights above 8 km ASL are strongly affected by noise which limits the comparability of both datasets. A comparison of samples near ground is limited by missing overlap correction of ACL data and the lack of background aerosol prediction data. The ash layers in heights between 2 km and 8 km ASL allow for identifying similar and non-similar structures of measurement and forward modeled COSMO-ART predictions of the Eyjafjallajökull ash. The maximum value of the (non-calibrated) ACL measured attenuated backscatter coefficient is by about 1 orders of magnitude lower than the attenuated backscatter coefficient from COSMO-ART prediction with BaLiFOp applied.

~~The same as Fig. 13 with a decreased volcanic ash number density. For this purpose, the ash number density predicted by COSMO-ART was reduced by factor 20 before applying the forward operator.~~